SCIENCE CHINA
Information Sciences

December 2019, Vol. 62 220402:1–220402:27
https://doi.org/10.1007/s11432-019-2642-6

• REVIEW •
Special Focus on Two-Dimensional Materials and Device Applications

The emerging ferroic orderings in two dimensions

Yupeng ZHANG[1†], Hanwen WANG[2,3†], Feng LI[1†], Xingdan SUN[2,3], Baojuan DONG[2,3], Xiaoxi LI[2,3], Zheng Vitto HAN[2,3,4*], Teng YANG[2,3*] & Han ZHANG[1*]

[1]*Institute of Microscale Optoelectronics, Shenzhen University, Shenzhen* 518060*, China;*
[2]*Shenyang National Laboratory for Materials Science, Institute of Metal Research, Chinese Academy of Sciences, Shenyang* 110016*, China;*
[3]*School of Material Science and Engineering, University of Science and Technology of China, Hefei* 230026*, China;*
[4]*Collaborative Innovation Center of Extreme Optics, Shanxi University, Taiyuan* 030006*, China*

Received 6 July 2019/Accepted 10 September 2019/Published online 13 November 2019

Abstract Because of the discovery of carbon atomic flatland, emerging physical phenomena are reported using the platform of two-dimensional materials and their hetero-structures. Especially, quantum orderings, such as superconductivity, ferromagnetism, and ferroelectricity in the atomically thin limit are cutting edge topics, which are of broad interest in the scope of condensed matter physics. In this study, we will recall the recent developments on two-dimensional ferroic orderings from both experimental and theoretical points of view. The booming of ferroic orderings in van der Waals two-dimensional materials are believed to hold promises for the next generation spin- or dipole-related nanoelectronics, because they can be seamlessly interfaced into heterostructures, and in principle are in line with large scale low-cost growth, flexible wearable devices, as well as semiconducting electronics thanks to the existence of band gaps in many of them.

Keywords two-dimensional materials, quantum orderings, magnetism, ferroelectricity, nanoelectronics

Citation Zhang Y P, Wang H W, Li F, et al. The emerging ferroic orderings in two dimensions. Sci China Inf Sci, 2019, 62(12): 220402, https://doi.org/10.1007/s11432-019-2642-6

1 Introduction

When thinned down to the two-dimensional (2D) limit, the electronic band structure of bulk van der Waals (vdW) materials may significantly change owing to the quantum confinement along the out-of-plane direction. This leads to the generation of abundant new electrical and optical phenomena with gate-tunability [1–6], as well as novel devices, which take advantage of the valley as a quantum degree of freedom [7–9]. These 2D materials also hold great promises in their applications in the fields of advanced nano-biomedicine and efficient energy conversion [10–14]. Furthermore, 2D vdW materials are often of a band gap, compatible with flexible devices [15], possible for large scale growth, which can strengthen up their functionalities once vertically and/or in-plane stacked/interfaced into a variety of heterostructures. Recently, persistence of quantum orderings such as superconductivity, magnetism, and ferroelectricity in the 2D limit has been widely investigated and it shows promising potential for future applications [16–22].

In this review, we will go through the recent developments of 2D ferroic orderings, including two major parts: (1) 2D magnetism and (2) 2D ferroelectricity. To the former group belong ferromagnetic (FM) and anti-ferromagnetic (AFM) vdW materials can be found and even persisted down to their monolayer limit, which have been confirmed by both experimental and/or theoretical evidences. While introducing the second group of material, the emerging novel ferroelectricity at the 2D limit is explained together with

* Corresponding author (email: vitto.han@gmail.com, yangteng@imr.ac.cn, hzhang@szu.edu.cn)
† These authors contribute equally to this work

a series of experimental and theoretical results. Ferroelectricity is indeed emerging as a quick-growing research topic related to ferroic ordering. This manifests tremendous opportunities in the development of fundamental physics and potential applications.

2 Magnetic ordering

2.1 Spin interactions

Magnetism in two-dimensions is introduced in several models over the last century, and it attracts a renewed interest in the last few years owing to the successful synthesis of a large family of van der Waals 2D atomic crystals, a truly 2D system, and the discovery of magnetism in some of them. However, a conflict appears. Long-range order in magnetic systems with continuous symmetry in 2D does not exist for a finite temperature within the isotropic Heisenberg model [23]; whereas such systems exhibit a phase transition at a finite temperature [24, 25]. Stanley and Kaplan [24] predicted in their numerical study that the anisotropic version of the Heisenberg model presents a phase transition. This hypothesis was later substantiated by the XY model defined by Berezinskii [26], Kosterlitz and Thouless [25]. Moreover, Fröhlich and Lieb [27] proved that a phase transition exists at a finite $T_{\rm C}$ in a variety of models with continuous symmetry in 2D. Because low-dimensional magnetism is then experimentally observed in real 2D systems, it deserves our much attention to look once more into the novel magnetic properties in the 2D systems. The simplest expression to describe the magnetic interaction is the quantum Heisenberg model, which is a special limit of the Hubbard model and can be expressed as follows:

$$\hat{H} = -\sum_{i \neq j} J_{ij} \boldsymbol{S}_i \cdot \boldsymbol{S}_j, \tag{1}$$

where J_{ij} corresponds to the exchange constant (integral) between the spins located on the i and j sites, and a many-body interaction summing over not only the nearest neighbors, but also over a large number of neighboring shells. The simplest and most used spin model is the Ising model where the spin vector exhibits only the $\pm z$-component. However, the elementary excitations such as a spin wave, are therefore suppressed. The rigorous solution of this equation generates a temperature dependence of magnetic moment for the 2D Ising model, such as

$$M(T) = \left(1 - \left(\sin h \frac{2J}{k_B T}\right)^{-4}\right)^{\frac{1}{8}} \tag{2}$$

for $T < T_{\rm C}$. The Curie temperature can be evaluated by

$$T_{\rm C} = \frac{2J}{k_B \ln(1 - \sqrt{2})}. \tag{3}$$

The XY model develops further by assuming a two-dimensional spin vector, and the expression of the Hamiltonian becomes

$$\hat{H}_{XY} = -\sum_{i \neq j} J_{ij} \boldsymbol{S}_i^x \cdot \boldsymbol{S}_j^y. \tag{4}$$

If going beyond the nearest neighboring interactions, the product of the spin operators becomes more difficult to calculate, and a possible way to solve this issue is to use a simplified mean-field solutions to the Heisenberg model [28], such as

$$\hat{H}_{\rm MF} = \sum_{i \neq j} J_{ij} \overline{S}_i \overline{S}_j - \sum_j \left[2 \sum_i J_{ij} \overline{S}_i\right] S_j. \tag{5}$$

In this case, the Curie temperature is thus given by

$$T_{\mathrm{C}} = \frac{2S(S+1)}{3Nk_B} \sum_{i \neq j} J_{ij}. \tag{6}$$

The strength of the spin interaction (J) arises from various coupling channels including direct exchange, super-exchange, double-exchange, itinerant (or Stoner, or RKKY) exchange depending on the environmental conditions. Direct exchange very often cannot be an important mechanism for the magnetic properties, simply because of the insufficient direct overlap between neighboring magnetic orbitals, especially for transition metal ions with localized d orbitals.

On the contrary, indirect exchange with non-magnetic ions as an intermediate plays a more essential role. One typical example is the super-exchange in ionic materials which involves ligand orbitals of negative ions (for example, oxygen or chalcogenide) as well as of transition metal atom. The competition between energy cost of making excited state (the Coulomb energy U) and a kinetic energy advantage (the electron hopping integral t) gives rise to an exchange $J \propto -t^2/U$. Such super-exchange depends strongly on the angle of the M-ligand-M bond [29]. For example, 180° gives rise to an antiferromagnetism in MnO, while 90° to a ferromagnetism in CrI_3 monolayer [30] and $Cr_2Ge_2Te_6$ (CGT) [31, 32].

Another example of indirect exchange is double-exchange, which appears in materials consisting of magnetic ions with mixed valency. The material $La_{1-x}Sr_xMnO_3$ with a mixing Mn^{3+} and Mn^{4+} oxidation state belongs to this group. In the 2D case, gate-tunable (enhanced) ferromagnetism in semiconductors such as CrI_3 and CGT may be relevant, and may introduce a valency mixture in the transition metal ions. Thus, the interplay between super-exchange and double-exchange mechanisms may play a relevant role in defining the properties of a material.

Both super-exchange and double-exchange are fostered by the presence of intermediate ligands, and usually appear in the ionic materials. In metals, the indirect exchange appears in its itinerant (delocalized) form. The exchange generated by localized magnetic moments, which are coupled with each other via the conduction electrons, is known as the RKKY type interaction. The coupling takes the form of distance-dependent exchange interaction given by

$$J_{\mathrm{RKKY}}(r) \propto \frac{\cos(2k_F r)}{r^3}. \tag{7}$$

The interaction is a long-range type and it oscillates within the distance r between the magnetic moments. Another case of itinerant exchange, also known as band ferromagnetism, occurs between the delocalized spins. The net magnetization is owing to spontaneously spin-split bands under the so-called Stoner condition. In this criterion, $U \cdot g(\mathrm{E_F}) \geqslant 1$ is satisfied. A strong Coulomb effect U, combined with a large electronic density of states $g(\mathrm{E_F})$ at the Fermi level, gives rise to a spontaneous ferromagnetism. This mechanism has been used in elemental ferromagnets including iron, nickel and cobalt. A similar behavior has also been reported in 2D metals, such as the magic-angle twisted bilayer graphene [33] and Fe_3GeTe_2 [34].

Based on these observations, the types of spin interactions are shown in Figure 1 and their characteristics are listed in Table 1 [30, 31, 35–51]. The generalized Heisenberg interaction can be used to describe most of the interactions, while a series of simplified/specific models are proposed to deal with dedicated cases, including Ising model, XY model, and those addressing indirect interactions in a variety of solid state systems. Apparently, when in a vdV material the out-of-plane dimension is folded and the system reaches the 2D limit, it exhibits magnetic characteristic. The major advantages of magnetism at 2D limit can be divided into two categories: on one hand, the possibility of twistable angles between two 2D vdW layers can lead to the unprecedented band engineering by manually shrink/expand the moiré super lattice—a scenario never observed in the 3D case. On the other hand, as summarized in Table 1, the spin interactions in 2D vdW materials can simply adapt to the 3D models, as described in the previous section. Most of the spin interaction models are still valid in 2D, while their advantage of tunability in both spin interaction and electronic properties provides an even wider platform for 2D spin and electronic-related devices. Moreover, the existence of band gaps provides tremendous opportunities in the improvement

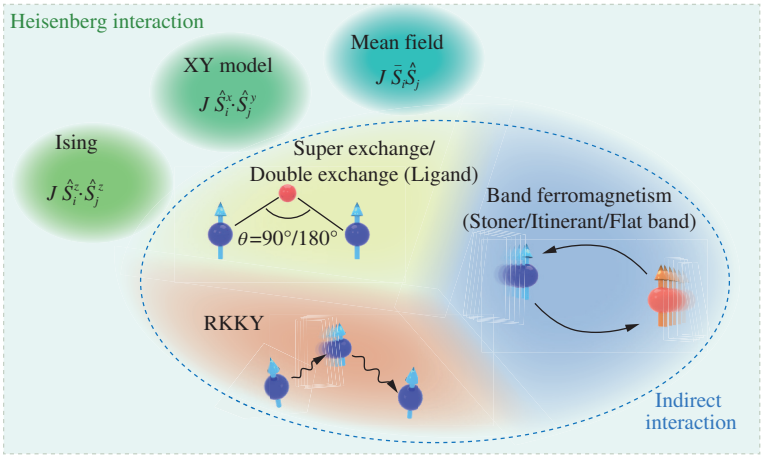

Figure 1 (Color online) Different types of magnetic interactions in three-dimensional (3D) crystals.

Table 1 2D magnets categorized according to the types of conventional 3D magnetic interactions shown in Figure 1

Model system		Indirect exchange	
Ising	CrI_3 [30,35] $CrBr_3$ [36,37] $CrCl_3$ [38–41]) $Cr_2Si_2Te_6$ [42] $FePS_3$ [43] $FePSe_3$ [44] Fe_3GeTe_2 [51]	Super-exchange/ Double-exchange/ Ligand	CrI_3 [45] $Cr_2Ge_2Te_6$ [46]
XY	$NiPS_3$ [47] $CoPS_3$ [48]	RKKY	Experimentally missing[a)]
Heisenberg	$Cr_2Ge_2Te_6$ [31] $MnPS_3$ [49] $MnPSe_3$ [50]	Stoner/Itinerant	Fe_3GeTe_2 [51]

a) Although some theoretical arguments may give hints to the existence of RKKY-type interactions in 2D materials [33, 34], it needs further clarifications.

of magnetic semiconducting spintronic applications. In the following subsections, the vdW 2D magnetic materials are introduced according to their electronic properties.

2.2 Metallic 2D magnetism

An important part of 2D magnetism is metallic magnetic materials, which have been confirmed by several experiments on a series of compounds, including Fe_3GeTe_2 (FGT) [51], V_5S_8 [52,53], and VSe_2 [54]. The 2D metallic FM ground state of vdW-layered V_5S_8 with T_C of ~8 K is reported by Niu et al. [53] by using a 3.2 nm sample, different from its bulk AFM ground state, whose T_N is estimated to be ~32 K [52], as shown in Figure 2(a)–(c). The thickness dependent FM ordering in metallic FGT is also reported by Deng et al. [51], whose T_C decreases from 180 K to 20 K when the sample passes from bulk to monolayer, as shown in Figure 2(d)–(e).

Owing to its vdW-layered structure, the 2D sample even down to monolayer is exfoliated by using Al_2O_3 associated method. Fei et al. [34] showed that the exchange interaction in FM FGT was Ising and itinerate for direct and super exchange interaction. In addition to its intrinsic magnetic properties, the magnetic order is also tunable. The T_C of a four-layer FGT is tuned from 120 K up to 310 K by using an ionic gate voltage of 2.1 V (Figure 2(f)). The long-range magnetic order in FGT is also indicated by the persisted Remnant Hall resistance (R_{xy}^r) at high temperature under an ionic gate voltage. Such gate tunable T_C is attributed to the gate induced Fermi level shifting according to the Stoner model.

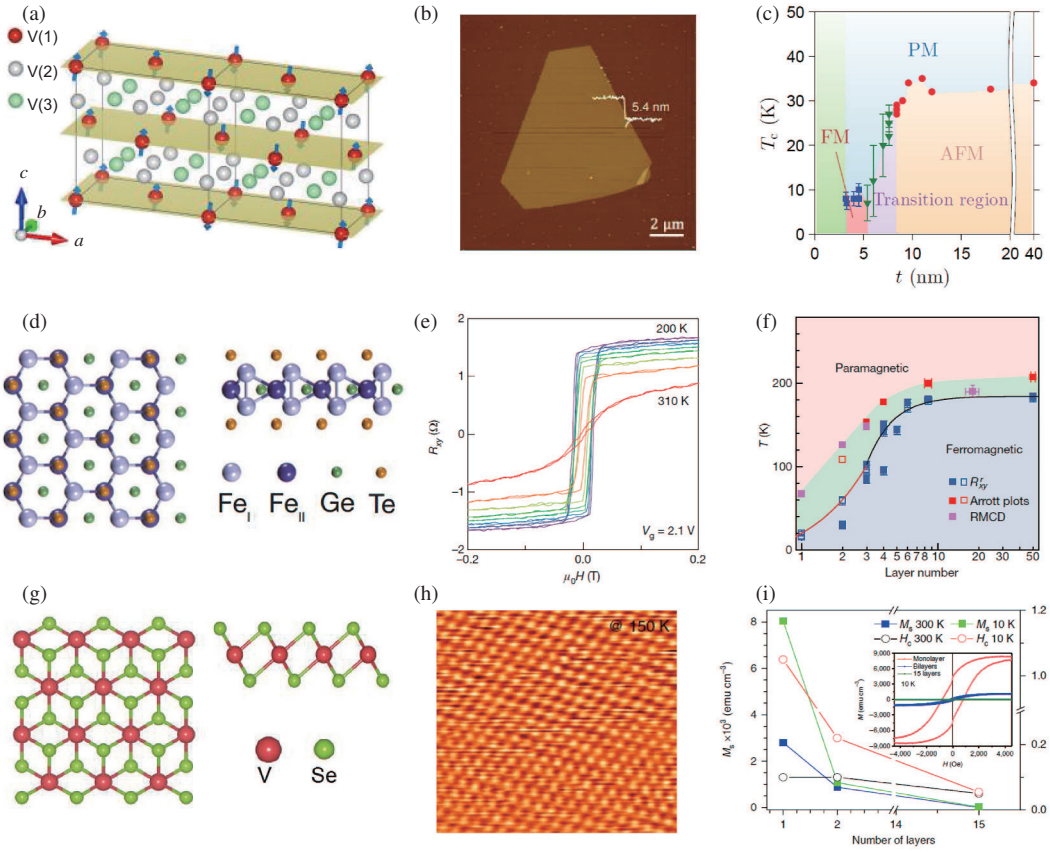

Figure 2 (Color online) Typical metallic magnetic vdW mateirlas. (a) The magnetic structure of layered V_5S_8. (b) Atomic force microscope (AFM is short for antiferromagnetic here in our study) topography of a typical V_5S_8 flake. (c) Critical temperature T_C-thickness t phase diagram. Reproduced from [53] @Copyright 2017 American Physical Society. (d) Schematic structure of layered Fe_3GeTe_2. (e) Phase diagram of FGT as number of layer and temperature. (f) R^r_{xy} of a four-layer FGT flake under a gate voltage of V_g = 2.1 V. Reproduced from [51] @Copyright 2018 Springer Nature. (g) Schematic structure of layered VSe_2. (h) STM images at 150 K. (i) Variations of Ms and Hc with the number of layers of VSe_2 film. The inset shows the M-H loops for the mono-, bi- and multilayer samples. Reproduced from [54] @Copyright 2018 Springer Nature.

Bonilla et al. [54] synthesized a 2D metallic FM VSe_2 with a bulk consisting of a paramagnetic vdW-layered material at T_C higher than 300 K by using the molecular beam epitaxy (MBE) method, as shown in Figure 2(g)–(i). A charge density wave (CDW) transition temperature is also confirmed in VSe_2. The ferromagnetic order in VeS_2 can be maintained up to room temperature and the magnetic moments of VSe_2 increase dramatically with a decrease in the thickness. Recently, Gong et al. [55] predicted that the AFM vdW bilayer VSe_2 can be transformed into a half metallic material by applying an electric field. The energy gap of spin-polarized states will be gradually closed and another energy gap will be opened owing to the Fermi level shifting to the constituent layers in the opposite directions.

Layered metallic magnetic compounds have shown their potential in revolutionizing the fabrication and functioning of spintronic devices [56, 57]. Wang et al. [58] studied the tunneling spin valves base on the device using a hexagonal boron nitride (h-BN) tunnel barrier and two ferromagnetic FGT electrodes. The anomalous Hall effect (AHE) characterizations show that FGT flakes with a thickness in the range of 6–50 nm behaved as metallic ferromagnets. The FGT/h-BN/FGT sandwiched devices can reach a tunneling magneto-resistance (TMR) up to 160% at 4.2 K, with a spin polarization of about 66%.

2.3 Semiconducting 2D magnetism in the CrX_3 family

Semiconducting magnetic materials exhibit broad application potential in the fields of inductor components, communication devices, and high-frequency microwave devices. Chromium trihalides (CrX_3, X =

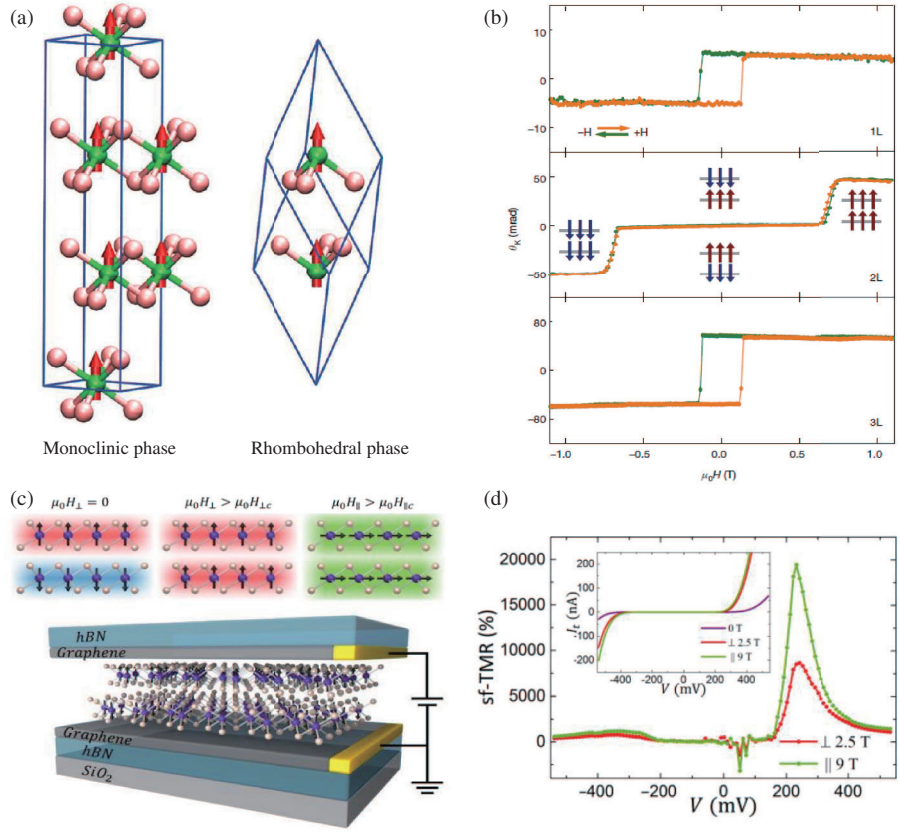

Figure 3 (Color online) Crystal structure of chromium trihalides CrX_3. (a) The monoclinic (left panel) and rhombohedral (right panel) phase of CrX_3. The red arrows represent the spin direction of Cr atoms. Reproduced from [63] @Copyright 2015 the Royal Society of Chemistry. (b) The magnetic behavior of monolayer, bilayer and trilayer CrI_3. Reproduced from [30] @Copyright 2017 Springer Nature. (c) Schematic of magnetic states in bilayer CrI_3 and schematic of 2D spin-filter magnetic tunnel junction (sf-MTJ). (d) sf-TMR ratio as a function of bias based on the I_t-V curves in the inset. Reproduced from [71] @Copyright 2017 Science Publishing Group.

Cl, Br, I) are typical semiconducting magnetic vdW materials, whose magnetic and electronic properties are not well understood until 2015. Figure 3(a) shows the structure of CrX_3, where Cr^{3+} ions are packed into hexagonal networks, where each Cr^{3+} ion is surrounded by six octahedral coordination X^- ions with thickness of 6–7 Å [59, 60]. Owing to the weak vdW interlayer interaction, CrX_3 is able to be exfoliated down to thin layer, and 2D magnetic semiconducting CrI_3 and $CrBr_3$ are studied by Huang et al. [30, 61] and Ghazaryan et al. [62], respectively. The first-principles calculations predict that the CrX_3 compounds may undergo a phase transition from a high temperature monoclinic structure with space group C2/m to a relative lower temperature rhombohedral phase with space group $R\overline{3}$, where two typical CrX_3 crystal structure is showed in Figure 3(a) [63]. Moreover, the calculations show that at room temperature the monoclinic phase CrI_3 is a semiconductor with a 1.2 eV band gap, and these predictions are in good agreement with the experimental optical band gap results [64]. Below Curie temperature, the rhombohedral phase CrI_3 behaves as an insulator [63] and can therefore be used as a magnetic tunneling barrier. The 61 K magnetic ordering temperature and strong magnetic anisotropy of the 2D CrX_3 have attracted much attention in recent years [65–69].

In 2015, McGuire et al. [70] obtained the crystallographic information in CrI_3 and confirmed the intrinsic ferromagnetic properties. Experimental results show that the T_C of CrI_3 is ∼61 K and its saturation magnetic moment is of 3.1 μ_B/Cr at about 2 K. First-principles calculations suggest that the robust ferromagnetism may persist down to monolayer CrI_3 and the Curie temperature may increase up to 130 K when a 10% in-plane tensile strain is applied [63]. According to their calculations, the magnetic anisotropy of the 2D CrI_3 is dominated by the intermediate I atoms due to the strong spin-orbit coupling,

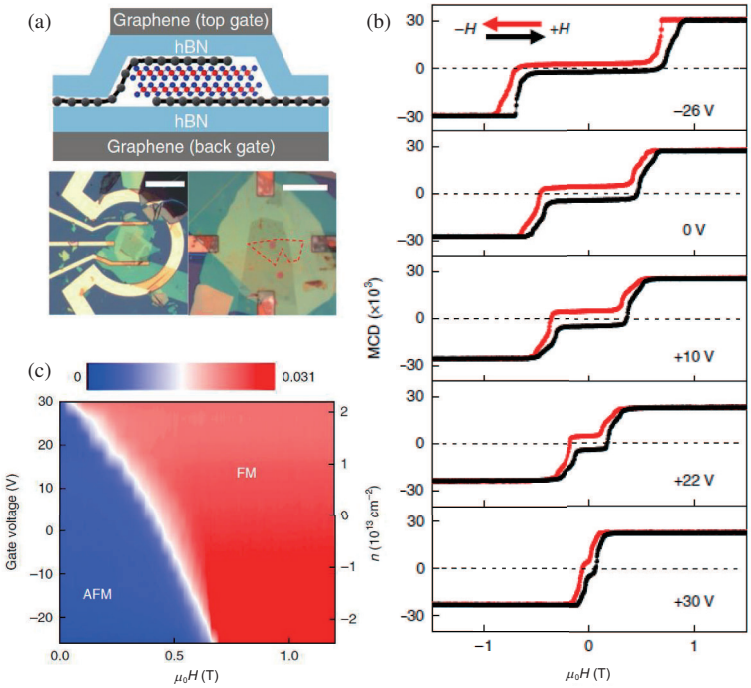

Figure 4 (Color online) Controlling magnetism in 2D CrI_3 by electrostatic doping. (a) A schematic side view and optical micrograph of a dual-gate bilayer CrI_3 field-effect device. (b) MCD versus magnetic field at 4 K at representative gate voltages. (c) Doping density-magnetic field phase diagram at 4 K. Reproduced from [74] @Copyright 2018 Springer Nature.

while the contribution from the Cr element is negligible.

Exfoliated 2D FM CrI_3 is firstly observed by Huang et al. [30] by using a magneto-optical Kerr effect (MOKE) microscopy. Monolayer CrI_3 is reported to be an Ising ferromagnetism with an out-of-plane spin orientation. Owing to the weak interlayer coupling interaction, its Curie temperature is found to be 45 K, which is only slightly lower than 61 K of its bulk form. Moreover, a layer-dependent magnetic order is investigated. It is found that monolayer, trilayer and bulk CrI_3 are ferromagnetic, whereas the bilayer CrI_3 is antiferromagnetic (Figure 3(b)). Because CrI_3 is rather insulating at low temperatures, the atomically thin CrI_3 tunnel layer between two metallic electrodes may be a good platform to investigate the spin-filter magnetic tunnel junction (sf-MTJ). Owing to the intrinsic intra-layer Ising ferromagnetic and inter-layer antiferromagnetic coupling of CrI_3, the TMR of few-layered CrI_3 based sf-MTJ may exhibit a multiple-level resistance as a function of an external perpendicular magnetic field, with graphite or few-layered graphene as tunneling electrodes (Figure 3(c)). The largest CrI_3 based spin-filtered TMR is in the order of 10^4, as shown in Figure 3(c)–(d) [71–73].

Atomically thin vdW materials provide a great platform to tune their electrical and optical properties and also to drive electronic phase transitions through electrostatic doping. Owing to the transparency and non-magnetic properties of graphene, the magnetic signal in the CrI_3 sample can be detected by MCD through two graphene gate electrodes spaced by h-BN dielectric (Figure 4(a)) [74]. For monolayer CrI_3, it is found that electrostatic doping significantly changes the saturation magnetization, coercivity, and T_C, thus exhibiting a magnetization-flipping field that increases/decreases with hole/electron doping in CrI_3.

Remarkably, by extrapolating the bilayer CrI_3 color map (Figure 4(b) and (c)) with an electron doping level of higher than $\sim 2.5\times10^{13}\mathrm{cm}^{-2}$, a transition from AFM to FM is observed without applying any external magnetic fields. These results reveal a strong inter-layer exchange coupling associated with doping, which enable a stable conversion of the magnetization in a bilayer CrI_3 with a purely electrical manner. In addition, the experiments also show the trend of tunneling current as a function of the gate voltage in a Gr/CrI_3/Gr three-layer tunneling structure. Even at 4 mV, a low bias induces a tunneling conductance effect in the device, which shows a bipolar feature with respect to the gate voltage, whereas

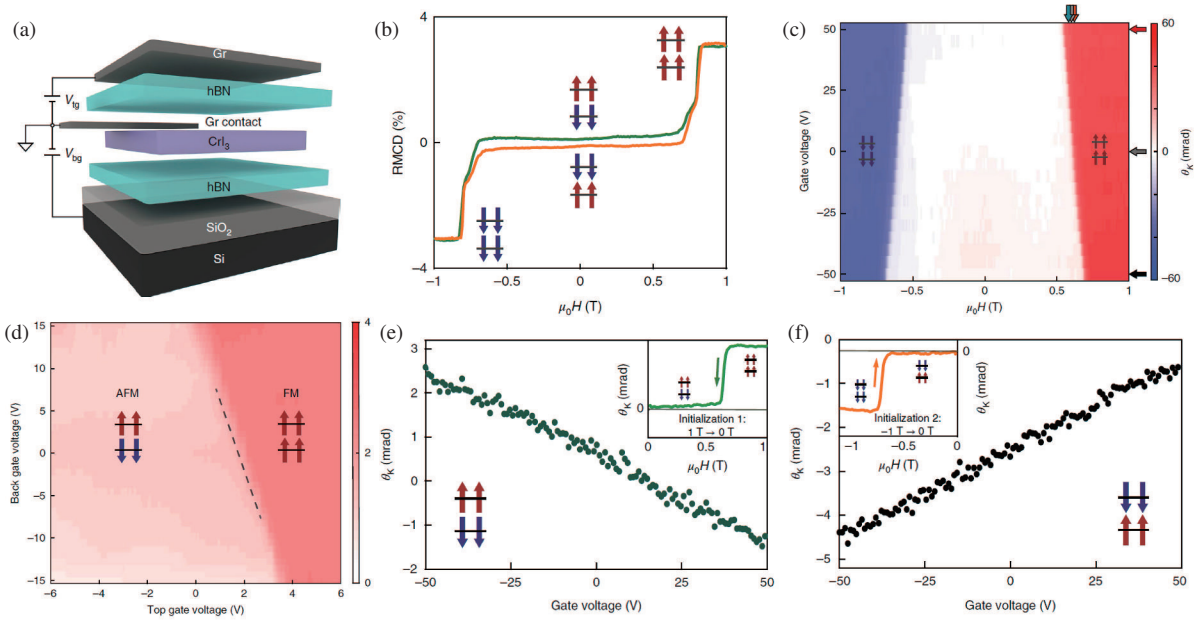

Figure 5 (Color online) Electrical control of 2D magnetism in bilayer CrI_3. (a) Schematic of a dual-gated bilayer CrI_3 device fabricated by vdW assembly. (b) RMCD signal of a bilayer CrI_3 device as a function of perpendicular magnetic field at zero gate voltage. (c) Intensity of the polar MOKE signal, θK, of a non-encapsulated bilayer CrI_3 device as a function of both gate voltage and applied magnetic field. (d) RMCD signal of a dual-gated device when sweeping both the graphite top gate and silicon back gate. Gate-dependent MOKE signal of a bilayer CrI_3 device prepared in the ↑↓ state (e) and in the ↓↑ state (f). Reproduced from [61] @Copyright 2018 Springer Nature.

its maximum conductance reaches 3 μS.

Similar phenomena are also reported almost in the same time [61, 75]. For example, in a bilayer CrI_3 device (Figure 5(a)), near the metamagnetic transition region, the gate voltage can alter the AFM to FM state transitions (Figure 5(b) and (c)). The full electrical control of the AFM states can be achieved in the absence of an external magnetic field (Figure 5(d)), despites this effect is rather weak. For the two AFM states, ↑↓ and ↓↑, the MOKE signal is linearly dependent on the gate voltage but with opposite trends, as shown in Figure 5(e) and (f).

As mentioned previously, ferromagnetic 2D CrI_3 has a theoretically predicted band gap of 1.2 eV, and it exhibits insulating properties below the Curie temperature in most of the experimental observations. The structural characteristics of $CrBr_3$ are similar to CrI_3, which exhibits similar magnetic properties. Ghazaryan et al. [62] developed a tunneling device based on the $CrBr_3$ barrier with an even number of layers, and graphene electrodes (Figure 6). The proximity-induced anisotropic magnetoresistance (PAMR) generated from the magnetization reversal process of the tunnel barrier is observed in the device (Figure 6(b)–(f)). The emergence of PAMR reveals the spin-orbit coupling and an exchange field in the graphene. The tunneling effect with magnon emission and proximity effects in the device may lead to a spin-filtered of tunnel current, which may provide new prospects in spintronics [76–78].

2.4 In-plane field effect transistors based on vdW magnetic semiconductors

It is well known that a conventional charge transistor based on semiconducting Si can realize an on/off state (the so-called logical computing capability) by controlling its electric field, owning to the change in the doping concentration of the semiconducting channel [79]. In addition to carrying a charge, electrons also have a fundamental spin property. A semiconductor having intrinsic magnetism has been long pursued: while the external electric field changes the Fermi surface, it also affects the arrangement of the spins, thus changing the macroscopic magnetic properties of the materials. In 1986, Story et al. [80] obtained a series of Mn-doped ferromagnetic PbSnTe materials, in which the Curie temperature is affected by the carrier concentration. This is the first experimental realization of a magnetically

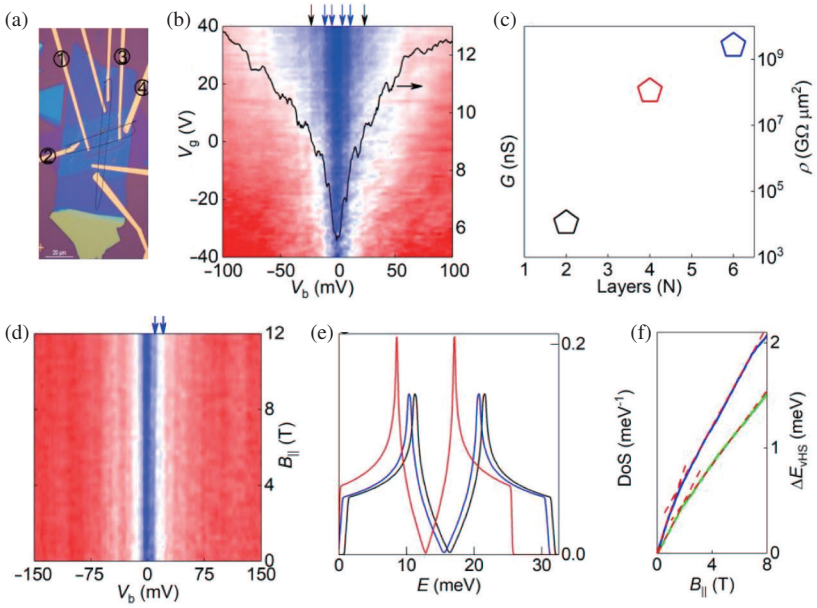

Figure 6 (Color online) Magnon-assisted tunneling in 2D $CrBr_3$ device. (a) Optical microscope image of 2D $CrBr_3$ device. (b) Zero-field differential tunneling conductance G dependence on the gate and bias voltages for the device. (c) Thickness dependence of the tunneling barrier on the resistivity of the device. (d) Differential tunneling conductance G as a function of B. (e) Calculated magnon density of states for $T = 10$ K, $B = 0$ T (blue line), $T = 10$ K, $B = 6.25$ T (black line), $T = T_C$, $B = 0$ T (red line). (f) Calculated changes of the position of the van Hove singularities in magnon density of states (e) as a function of magnetic field for temperatures close to T_C. Reproduced from [62] @Copyright 2018 Springer Nature.

doped semiconductor. In 2000, Ohno and Chiba [81] prepared the Mn-doped InAs, and achieved the controllability of the anomalous Hall effect by using an electric field for the first time. Such systems are commonly known as diluted magnetic semiconductors (DMSs). After the publication of the first DMS work, magnetic semiconductors have been widely studied in bulk materials. It is of great importance to now re-consider such systems in the 2D electronic field.

In 2015, Sivadas et al. [82] investigated the magnetic ground states of a monolayer of transition-metal chalcogenides by using first-principles calculations based on the density functional theory. The ground-state phase of the ABX_3 compounds modulate by the Heisenberg model. The results show that the monolayer $CrGeTe_3$ is a ferromagnet with a Curie temperature of 106 K, the monolayer $CrSiTe_3$, $MnPS_3$ and $MnPSe_3$ are present antiferromagnet properties, while a uniform in-plane tensile strain of ∼3% can be used to tune the magnetic ground state of monolayer $CrSiTe_3$ into a ferromagnetic state, with a Curie temperature of 111 K. The layered $Cr_2Ge_2Te_6$, with space group of C2/m [83], belongs to a class of ferromagnetic semiconductors and can be exfoliated down to the 2D limit [84]. The Cr atoms form a distorted honeycomb lattice and are octahedrally coordinated by six Te atoms with its three neighboring ligands. Moreover, the centers of these hexagons are occupied by the B2 groups. Due to this configuration, the monolayer $Cr_2Ge_2Te_6$ is stable [46].

In 2016, Zhang et al. [85] found magnetic anisotropy and the insulating property below Curie temperature in single-crystalline $Cr_2Ge_2Te_6$. Tian et al. [86] revealed the presence of strong spin-phonon coupling effects and observed the magnetic quasi elastic scattering in $Cr_2Ge_2Te_6$ via Raman scattering under the temperature between 10 and 325 K. In 2017, They also reported the preparation and characterization of a 2D ferromagnetic $Cr_2Ge_2Te_6$ with a thickness in the range of 3–40 nm [83]. A magnetic hysteresis loop is observed in the 40 nm $Cr_2Ge_2Te_6$ flake at 3 K, whereas its Curie temperature is higher than 60 K. They further demonstrate the giant modulation of the channel resistance of 2D $Cr_2Ge_2Te_6$ devices via the electric field effect.

In order to eliminate the effects of air-degradation on 2D $Cr_2Ge_2Te_6$, Wang et al. [32] employed thin h-BN as protecting layers to encapsulate a 3.5 nm $Cr_2Ge_2Te_6$ field effect transistor with two graphene

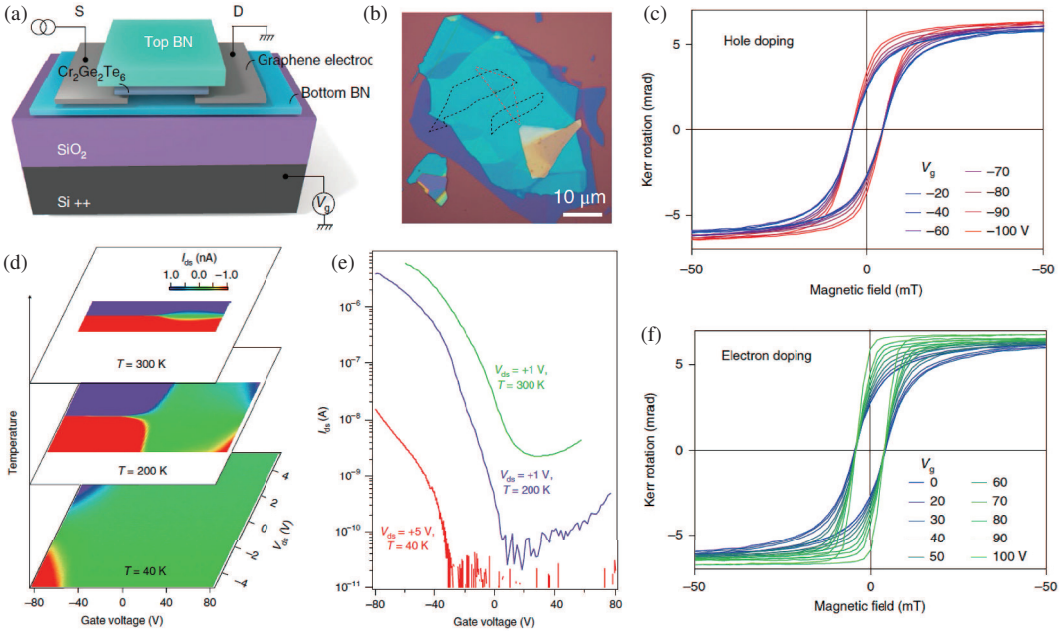

Figure 7 (Color online) Electric-field control of magnetism of 2D semiconducting $Cr_2Ge_2Te_6$. (a) Schematic of a few-layered $Cr_2Ge_2Te_6$ flake encapsulated by two h-BN layers, contacted via graphene electrodes. (b) Optical image of the device. (c) Colour map of I-V curves as a function of gate voltage at different temperatures. (d) Field effect curves of the device with different V_{ds} and temperatures. Kerr angle measured at 40 K for negative (e) and positive (f) gate voltages respectively. Reproduced from [32] @Copyright 2018 Springer Nature.

electrodes (Figure 7(a) and (b)). The electrical transport measurements show that the $Cr_2Ge_2Te_6$ remains conducting below the ferromagnetic Curie temperature (∼64 K), as reported in Figure 7(c). Interestingly, it behaves as an ambipolar field effect transistor where both electron- and hole-side conduct. The bipolar field effect consists of a planar FET with a maximum on-off ratio of 10^4, which is different from the value of the bipolar conductance in the CrI_3 tunneling junction structure [73]. The room temperature carrier mobility of such FET is estimated to be 50–100 cm^2/Vs. The transfer curves are shown in Figure 8(d). However, low temperature carrier mobility of this device is extremely low. The low-temperature micro-domain magneto-optical Kerr measurement below the Curie temperature shows that the magnetic properties of the device can be effectively tuned by applying a gate voltage in a bipolar manner (Figure 7(e)–(f)). Simulations suggest a spin-polarized energy band in the system, and the bipolar field effect of spin and charge is owing to the spin majority band is contributed by the p orbital of Te atoms at bands valence band maximum and spin minority is contributed by the d orbitals of Cr atoms in conduction band minimum.

In addition, the effect of strain on the magnetism of 2D ferromagnetic semiconductor $Cr_2Ge_2Se_6$ is predicted by the DFT calculations. The results show that the Curie temperature T_C increases with the increase of the strain and reaches to room temperature by applying a 3% strain. The anomalous Hall conductivity in 2D $Cr_2Ge_2Se_6$ and $Cr_2Ge_2Te_6$ is predicted to be comparable to Fe and Ni. Two mechanisms may account for such enhanced value of T_C by strain. (1) The enhanced direct antiferromagnetic coupling between Se/Te and Cr, and (2) the enhanced ferromagnetic coupling [87]. The magnetic, electronic, and photoelectric properties of 2D $Cr_2Ge_2Se_6$ also have been studied by other group recently [88–91].

Miao et al. [92] proposed a new way to obtain intrinsic ferromagnetic semiconductors by reducing the bulk antiferromagnetic properties in CrOX vdW semiconductors to their 2D limit (Figure 8(a)). The results of the first-principles calculations and the molecular dynamics simulations prove that the single-layered CrOCl and CrOBr are intrinsic ferromagnetic semiconductors with their predicted Curie temperature of 160 K and 129 K, respectively, as shown in Figure 8(b). In addition, under appropriate strains, the T_C of the CrOX monolayers can be enhanced up to 204 K. The magneto crystalline anisotropy energy has the same order of those of Fe and Co. The calculated results also indicate that the 2D CrOCl

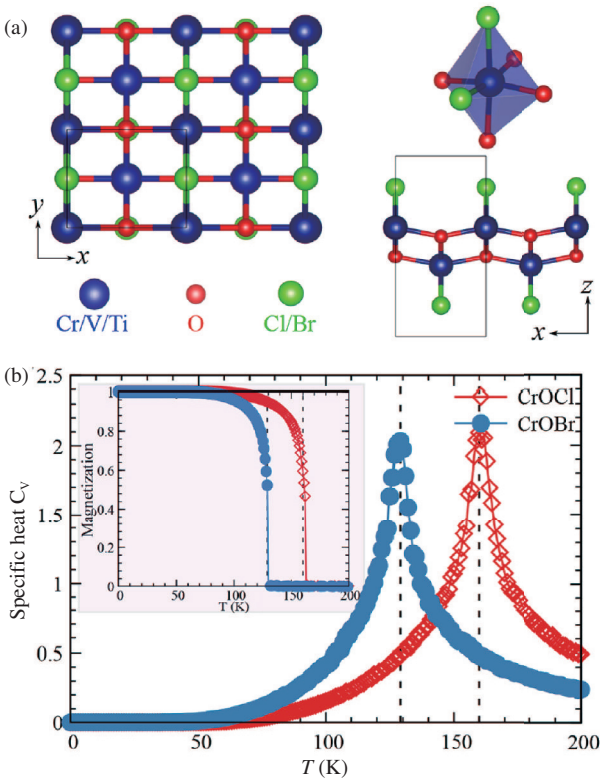

Figure 8 (Color online) Magnetic properties of CrOCl and CrOBr monolayers. (a) Crystal structures of transition-metal oxyhalides. (b) Specific heat CV with respective to temperature for the CrOCl and CrOBr monolayers and the inset shows the corresponding magnetization. Reproduced from [92] @Copyright 2018 American Chemical Society.

and CrOBr crystals are highly stable at room temperature and easily prepare from their bulk forms by using the mechanical peeling method. It is noteworthy that the band gaps of monolayer CrOCl and CrOBr are 2.38 and 1.59 eV, respectively.

Recently, a new class of 2D metal phosphorus chalcogenides (XPS), including $NiPS_3$, $FePS_3$ and $CoPS_3$, has attracted increasing attention for its semiconducting and magnetic properties. Lançon et al. [93] studied the neutron inelastic scattering in a quasi 2D $NiPS_3$ in order to understand its magnetic exchange interactions and magnetic anisotropy. The results show that the $NiPS_3$ is antiferromagnetic and with a small anisotropy, which leads to the generation of dispersive magnons with a ∼7 meV gap. Rehman et al. [94] synthesized the 2D layered $MnPS_3$ and $FePS_3$ materials by chemical vapor transport method. The magnetic properties of multilayer $MnPS_3$ and $FePS_3$ materials are investigated. These two materials exhibit an antiferromagnetic behavior, with the antiferromagnetic transition temperature of 78 K and 123 K for the $MnPS_3$ and $FePS_3$ crystals, respectively. The insulator-metal transition under different pressure is also observed in the bulk $FePS_3$ by electrical transport measurements [95].

Kim et al. [96] reported in $NiPS_3$ (Figure 9(a) and (b)), from bulk down to bilayer, a persisting antiferromagnetic order, which however is drastically suppressed in the monolayer limit. The variation of two-magnon Raman scattering as the function of the thickness is also investigated (Figure 9(c)). Interestingly, the Néel temperature decreases upon the decrease of the sample thickness (Figure 9(d)). The thickness dependence strongly indicates that the intra-layer exchange interactions are much stronger than the interlayer ones.

The layered transition metal phosphorus chalcogenides (TMPCs)-$CuMP_2X_6$ (M = Cr, V; X = S, Se) is another class of semiconductors with the band gap ranging from 0.9 eV to 1.4 eV. Qi et al. [97] predicted that the ferromagnetism and ferroelectricity can coexist in monolayer (TMPCs)-$CuMP_2X_6$ based on density functional theory calculations. The spontaneous polarization of ferroelectricity in these monolayer materials is produced by the nontrivial electric dipole moment, which originates from the off

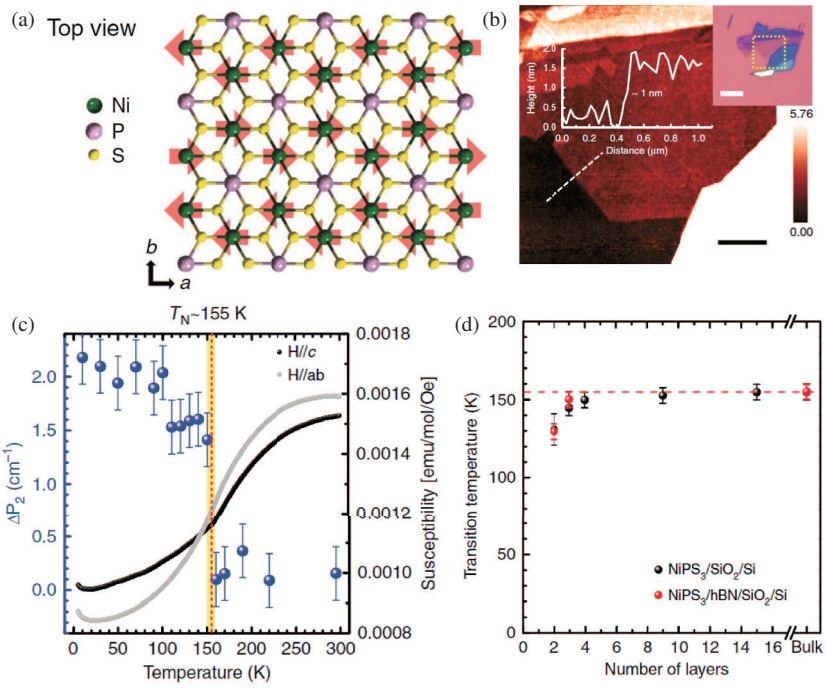

Figure 9 (Color online) Layer dependence magnetic properties of $NiPS_3$. (a) Crystal structure of $NiPS_3$. (b) Optical and atomic force microscope image of the sample. (c) Temperature dependences of phonon frequency difference and susceptibility of bulk $NiPS_3$. (d) Thickness dependence of Néel temperature for few-layer $NiPS_3$. Reproduced from [96] @Copyright 2019 Springer Nature.

center of Cu atoms. The FM order comes from indirect exchange interaction between the Cr and the V atoms, and it is more stable than the AFM order.

2.5 Extrinsic magnetic 2D vdW materials

Magnetic doping plays a significant role in functionalizing low dimensional materials of emerging spintronics, especially in the field of magnetic semiconductors. In addition, 2D transition metal dichalcogenides (TMDs) have attracted a significant attention in optoelectronics, sensor, catalysis and energy fields. Recently, the ferromagnetic doping of 2D TMD materials has attracted an growing interest.

For instant, magnetic ordering has been discovered in the line and point defects of 2D MoS_2 [98]. Theoretical calculations also show that elemental (such as V, Mn, Fe, Co, and Cu) doping can turn a single layer MoS_2 into ferromagnetic. Moreover, when the thickness exceeds one layer, it becomes antiferromagnetic [99–102]. Xia et al. [103] reported a 5% Cu doped MoS_2 nanosheets prepared by the hydrothermal method. The nanosheets present ferromagnetism properties in the temperature range of 300–930 K, with a total magnetic moment in the range of 0.0246–0.006 emu·g^{-1}. The Curie temperature reaches up to 930 K. Wang et al. [104] obtained Mn, Fe, Ni, and Co doped multi-layer MoS_2 by using a low-energy ion implanter facility. The saturation magnetization of 1% Mn doped MoS_2 is reported to be 20 kOe, indicating the present of a ferromagnetic phase. The ferromagnetic ordering is observed at room temperature in 4% Co and 4% Fe doped MoS_2, while the 4% Ni doped MoS_2 does not exhibit room temperature ferromagnetism.

However, the early reported magnetic doping experiments in TMDs are carried out on multilayer nanosheets, which are rather close to the bulk limit. Recently, Li et al. [105] used the traditional chemical vapor transport method to obtain high-quality Fe-SnS_2 single crystals with different Fe doping concentrations, from which they obtain monolayer Fe-SnS_2 nanosheets via mechanical exfoliation (Figure 10). Field effect transistor based on monolayer $Fe_{0.021}Sn_{0.979}S_2$ is studied as well as its optical response. The Fe-SnS_2 shows to have a potential in the development of novel nanoelectronics, magnetic and optoelectronics applications. By using chemical route, weak FM ordering at room temperature is also reported

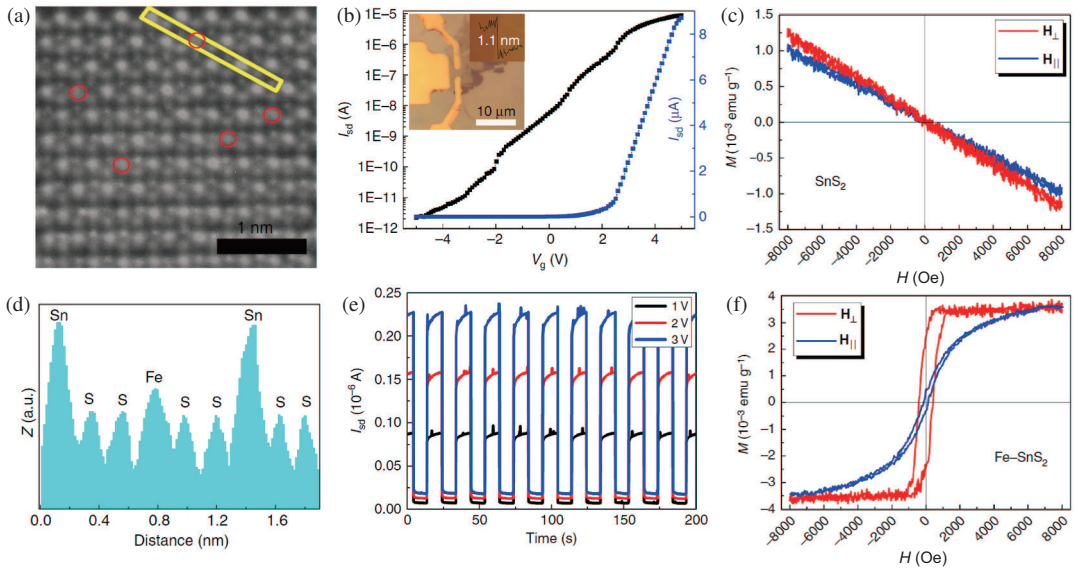

Figure 10 (Color online) Fe-doped 2D SnS_2 magnetic semiconductor. (a) High-resolution scanning transmission electron microscopy (STEM) image of the $Fe_{0.021}Sn_{0.979}S_2$ flake; the red circles are Fe atoms. (b) Z-contrast mapping in the areas marked with yellow rectangles in (a). Electrical characteristics (c) and photo response (d) of the monolayer $Fe_{0.021}Sn_{0.979}S_2$ device. Magnetic hysteresis loops for SnS_2 (e) and $Fe_{0.021}Sn_{0.979}S_2$ (f) at 2 K using VSM, respectively. Reproduced from [105] @Copyright 2018 Springer Nature.

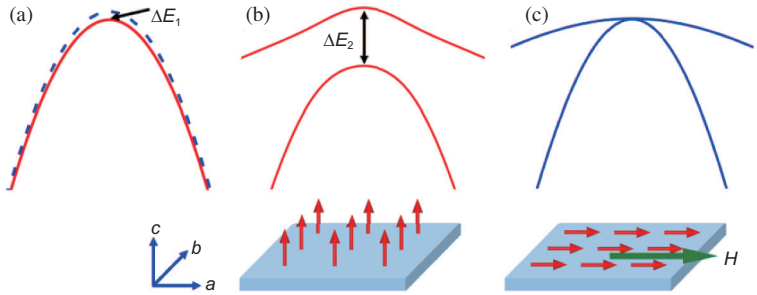

Figure 11 (Color online) Schematic view of Zeeman effect and giant magneto band structure effect. (a) External magnetic field induced Zeeman splitting of a specific band. Calculated band splitting using toy model for a 2D system with (b) magnetization along out-of-plane c axis (M//c), and (c) rearranged magnetization along in-plane axis (M//a) by applying a magnetic field H. Reproduced from [107] @Copyright 2018 American Chemical Society.

in h-BN with 8.1% fluorination, and a saturation magnetism of 0.018 emu (electromagnetic units) $\cdot g^{-1}$ can be obtained [106].

So far, the existing reports on transition metal doped ferromagnetic TMDs are based on multi-layer MoS_2 nanosheets and their transport and optoelectrical performances have yet to been optimized. The studies on a controllable ferromagnetic doping of single-layer crystal are missing, and the development of novel, facile, and more precise doping techniques is required.

2.6 Other novel magnetic properties in 2D systems

It is recently found that, in 2D CrI_3 crystal, a large magnetron electronic structure effect can exist, according to the density functional theory calculations [107]. When the magnetization direction is controlled from the out-of-plane to the in-plane, the electron band structure changes from a direct band gap to an indirect band gap via the spin-orbit coupling. Moreover, the Fermi surface changes as well. The theory predicts that the energy regulation of the external magnetic field on the electronic band structure can reach up to 0.1 eV, which is three orders of magnitude larger than the classical Zeeman coupling (Figure 11). In addition, changes in the magnetization direction can also drive topological phase transitions.

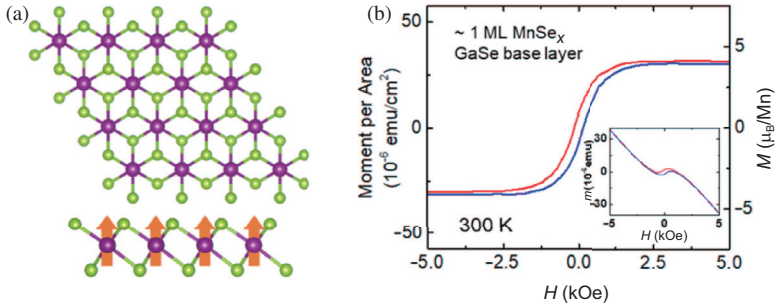

Figure 12 (Color online) Intrinsic ferromagnetism in 2D $MnSe_x$. (a) Top and side views of $MnSe_2$ lattice. (b) Magnetic hysteresis loop of monolayer $MnSe_x$. Reproduced from [108] @Copyright 2018 American Chemical Society.

These significant changes in the band gap can modify the optical and electrical transport properties. For example, a magnetic field can be used to control the magnetization direction of the fluorescence effect. In addition, the variation of the Fermi surface induces a large anisotropic magnetoresistance, which modifies the topological properties of the surface state of the material.

O'Hara et al. [108] obtained the 2D ferromagnetic and wide band-gap semiconductor manganese selenide crystal (Figure 12(a)) by using molecular beam epitaxy (MBE). The ferromagnetic hysteresis loops in Figure 12(b) are tested on a superconducting quantum interference device magnetometry at room temperature and observed intrinsic ferromagnetism in MnSex. The results show that a coercivity of 1 ML MnSex on the GaSe substrate is 150 Oe and 100 Oe, and the saturation magnetic moments are ∼3.3 $\times$ 10^{-5} emu·cm^{-2} and ∼3.2 $\times$ 10^{-5} emu·cm^{-2}, respectively. They attribute the ferromagnetic ordering to the interface between α-$MnSe_x$/GaSe or surface of α-$MnSe_x$(111), while there is no difference of two mechanisms for monolayer sample.

Mounet and his colleagues [109] developed a geometrical algorithm based on big data high-throughput screening to "peel" two-dimensional materials. They start from a poor of more than 100000 3D compounds with known structure information from inorganic crystal structure database (ICSD) or the crystallographic open database (COD). The researchers first screen 5619 materials with two-dimensional layered structural units. Further, through the vdW DFT calculation, 1825 low exfoliation energy materials are identified. Among them, 1036 materials have a new structural model. The researchers analyzed the electrical, magnetic, vibration, and topological structures of 258 compounds, confirming 56 easily prepared 2D ferromagnetic and antiferromagnetic materials finally, including half metal and half-semiconductors, as show in Figure 13. This library will guide for the exploration of more two-dimensional crystals, especially for magnetic materials.

A list of known experimental 2D magnetic materials and their properties is shown in Table 2 [30, 32, 51, 53, 54, 61, 74, 94, 96, 105, 106, 108, 110–112]. The properties, according to the to-date experimental progress, listed in Table 2 and are extracted from single layer materials. Importantly, there are only a few magnetic semiconductors in the list, while the Curie temperatures are very low and the transport performance is very poor below the Curie temperature. Currently, room temperature 2D ferromagnetic materials (Fe_3GeTe_2 [51], VSe_2 [54], $CrTe_2$ [110]) are mostly metallic in nature, which means that they are unlikely to be gate-tunable for transistor operations. Room temperature semiconducting ferromagnetic vdW materials still have to be discovered.

Tong et al. [113] explored the skyrmion in 2D ferromagnetic monolayer materials on bulk antiferromagnetic substrates. The skyrmions originate from a lateral modulation of the interlayer magnetic coupling by the locally different atomic registries in a moiré superlattice. The moiré-induced skyrmions are doubly degenerated with opposite topological charges and the moiré periodicity that can be tuned by strain and interlayer translation. The ground state of the moiré superlattice is skyrmion when the interlayer coupling is strong enough, while it is metastable skyrmion excitation when the interlayer coupling is relative weak. These results point to potential uses of moiré skyrmions both as information carriers and as tunable topological background of electronic transport.

(a)

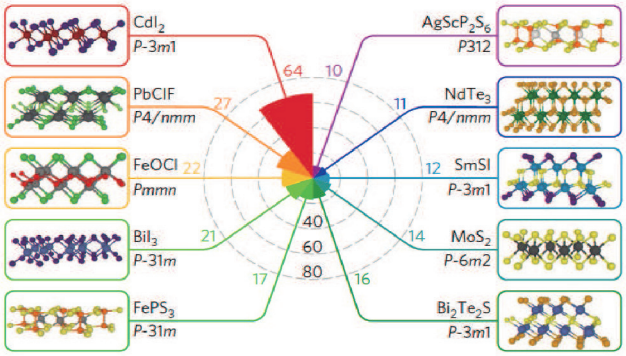

(b)

	Ferromagnetic	Antiferromagnetic
Metals	$Co(OH)_2$, CoO_2, ErHCl, ErSeI, EuOBr, EuOI, $FeBr_2$, FeI_2, FeTe, LaCl, NdOBr, PrOBr, ScCl, SmOBr, SmSI, TbBr, TmI_2, TmOI, VS_2, VSe_2, VTe_2, YCl, YbOBr, YbOCl	CoI_2, $CrSe_2$, FeO_2, FeOCl, FeSe, PrOI, VOBr
Semiconductors	CdOCl, $CoBr_2$, $CoCl_2$, CrOBr, CrOCl, CrSBr, $CuCl_2$, ErSCl, HoSI, $LaBr_2$, $NiBr_2$, $NiCl_2$, NiI_2	$CrBr_2$, CrI_2, LaBr, $Mn(OH)_2$, $MnBr_2$, $MnCl_2$, MnI_2, VBr_2, VCl_2, VI_2, $VOBr_2$, $VOCl_2$

Figure 13 (Color online) Data base of 2D easily exfoliatable magnetic materials. (a) The polar histogram of most common 2D structural prototypes include 1036 easily exfoliatable 2D materials. (b) Easily exfoliatable magnetic compounds. Reproduced from [109] @Copyright 2018 Springer Nature.

Table 2 The magnetic properties of known experimental 2D magnetic materials

	Materials	FM/AFM	Curie/Neel temperature	Gap	Ref.
Fe_3GeTe_2 family	Fe_3GeTe_2	FM	20 K	Metallic	[51]
$CrGeTe_3$ family	$Cr_2Ge_2Te_6$	FM	64 K	–	[32]
	$Cr_2Si_2Te_6$	FM	80 K	0.4 eV/1.2 eV	[111]
XPS family	$FePS_3$	AFM	123 K	1.5 eV	[94]
	$MnPS_3$	AFM	78 K	2.4 eV	[94]
	$NiPS_3$	AFM	130 K	–	[96]
CrI_3 family	Odd-layer CrI_3	FM	45 K	Semiconducting	[30]
	Even-layer CrI_3	AFM	45 K	Semiconducting	[61]
	$CrBr_3$	FM	37 K	Semiconducting	[74]
	VI_3	FM	49 K	0.6 eV	[112]
Others	V_5S_8	AFM	8 K	Metallic	[53]
	VSe_2	FM	300 K	Metallic	[54]
	Fe-SnS_2	FM	31 K	2.2 eV	[105]
	Fluorinated h-BN	FM	–	Semiconducting	[106]
	$MnSe_x$	FM	300 K	Semiconducting	[108]
	1T-$CrTe_2$	FM	310 K	Metallic	[110]

3 Ferro-electricity in the 2D limit

Similarly to the spin alignment in magnetic materials, the spontaneous alignment of electric dipole with the electric dipole polarizations can be mostly found in insulating materials, behaving in a ferroic way. This phenomenon shows hysteresis loops relative to the direction of the externally applied electric field. Ferroelectricity is considered as a collective property of the material, which has a great potential in many practical applications, such as non-volatile memories [114], transducers [115], and sensors [116]. The development of traditional ferroelectrics, such as perovskites (PZT, BTO) and polyvinylidene difluoride

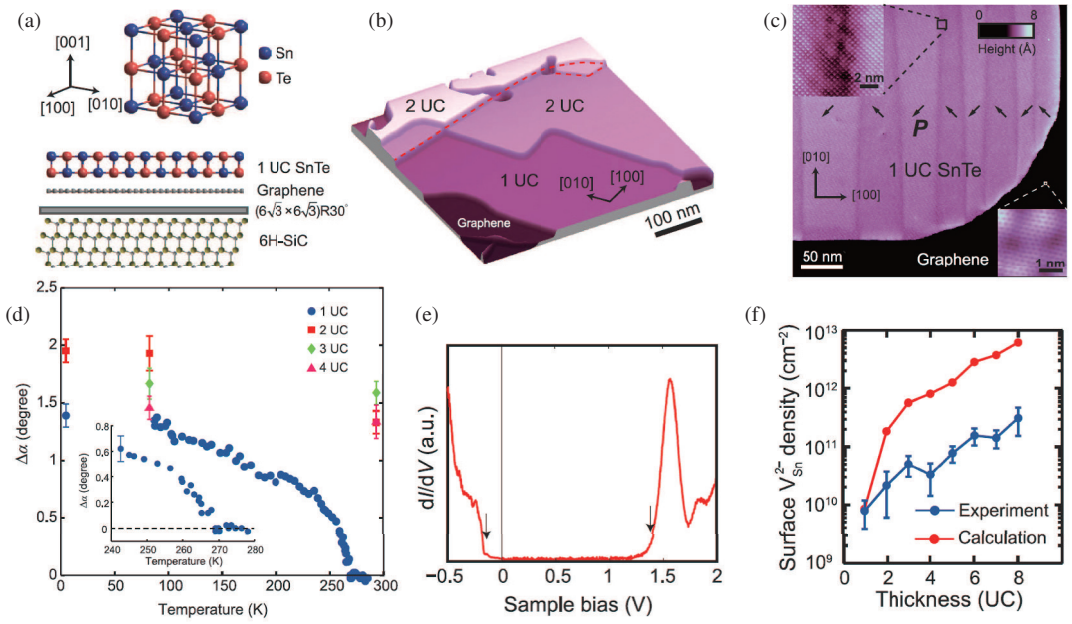

Figure 14 (Color online) In-plane ferroelectricity in 2D SnTe. (a) Schematics of the SnTe crystal structure (upper) and the SnTe film (lower). (b) Typical STM topography image of SnTe film. The red dotted line indicates the steps of substrate. (c) The stripe domain of a 1-UC SnTe film. The arrow in each domain indicate the direction of lattice distortion. (d) Temperature dependence of the distortion angle for the 1- to 4-UC SnTe films. (e) The dI/dV spectra acquired on the surface of a 1-UC film at 4.7 K. The arrows indicate the edges of the valence and conduction bands. The peak at 1.5 V corresponds to a van Hove singularity in the conduction band. (f) Thickness dependence of Sn vacancy density at the growth temperature of 450 K. Reproduced from [123] @Copyright 2016 Science Publishing Group.

(PVDF), to fabricate nanoscale devices is rather limited, because the ferroelectricity will be difficult to survive in ultrathin films owing to the depolarization fields. Moreover, because the interfacial defects and mismatch strains deteriorate or even destroy the ferroelectricity [117–121], the epitaxial growth of these FE materials requires very restricted conditions, which therefore hinders their commercial applications.

Recently, the rise of 2D vdW ferroelectric (FE) materials with a dangling-bond-free surface and weak interlayer interactions may provide a new pathway to eliminate these aforementioned limitations. Moreover, compared with traditional ferroelectrics with a large bandgap and a low carrier mobility, many 2D FE materials are reported to be semiconducting with a tunable bandgap and a high mobility. This is of great importance in semiconductor industry. Here we will recall some of the recent experimental studies on 2D ferroelectric orderings.

Bulk SnTe possesses a rock-salt structure at room temperature. Below ∼98 K, the crystal undergoes a cubic-to-rhombohedral structural phase transition with the two sublattices consisting of Sn and Te atoms displaced from each other along the ⟨111⟩ direction, in this fashion, the ferroelectric state can be found [122]. Chang et al. [123] employed graphene as a buffer layer for the epitaxial growth of SnTe film (Figure 14(a)), stable in-plane ferroelectricity is observed in atomic-thick SnTe film down to a 1-unit cell (UC) limit. Figure 14(b) shows the scanning tunneling microscopy (STM) topography images of such SnTe films. The weak vdW interaction between the SnTe film and graphene greatly reduces the strain effect and stabilizes the spontaneous polarization. Figure 14(c) reveals the stripe-shaped domain in the 1-UC SnTe film as evidenced by scanning transmission electron microscopy (STEM). By carefully controlling the substrate temperature and the SnTe flux, the Sn vacancy density is suppressed to 10^{10} and 10^{11} cm^{-2} for the 2-UC film and even lower for the 1-UC SnTe film, which helps to reduce the charge screening effect. Surprisingly, the ferroelectric transition temperature T_C of the 1-UC SnTe film reaches as high as 270 K and is above room temperature for the 2- to 4-UC films (Figure 14(d)). They attribute such strong enhancement in ferroelectricity of the SnTe atomically-thin films to the decrease of the screening charge and the increase of the band gap (Figure 14(e) and (f)).

To investigate the origin of such enhancement in ferroelectricity of SnTe ultrathin films, Liu et al. [124]

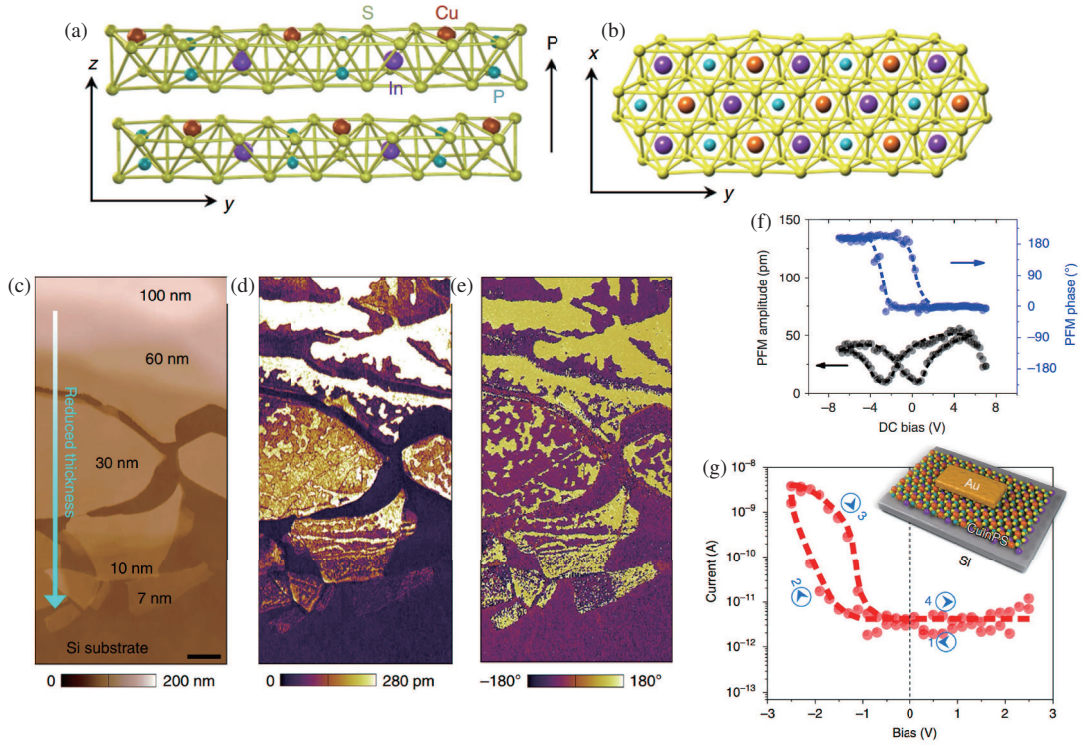

Figure 15 (Color online) Crystal structure and the ferroelectric characters of CIPS flakes. The side view (a) and top view (b) for the crystal structure of CIPS with vdW gap between the layers. Within a layer, the Cu, In and P-P form separate triangular networks. Reproduced from [127] @Copyright 1998 American Physical Society. The polarization direction is indicated in by the arrow. AFM topography (c) PFM amplitude (d) and PFM phase (e) for CIPS flakes ranging from 100 to 7 nm thick, on doped Si substrate. Scale bar in (c) is 1 μm. (f) The PFM amplitude (black) and phase (blue) hysteresis loop for a 4 nm CIPS flake. (g) The *I*-*V* curves from the Si/CIPS (30 nm)/Au heterostructure. Inset is the schematic of the device. Reproduced from [130] @Copyright 2016 Springer Nature.

carried out first principles calculations in defect-free SnTe thin films. They found that, due to a subtle interplay between the hybridization interactions (HIs) and the Pauli repulsions (PRs), the ferroelectric switching energy barrier in SnTe thin film is larger than that in bulk SnTe when the thickness is larger than 2 UC, and the 5-UC SnTe film possesses the largest energy barrier. Such non-monotonic dependency is also confirmed by Hong group [125].

Copper indium thiophosphate, CuInP2S6 (CIPS), is another vdW layered material exhibiting room-temperature ferroelectricity [126]. It is a collinear two-sublattice ferrielectric system containing polar CuI and InIII sublattices (Figure 15(a) and (b)). When the temperature drops below T_{C} (~315 K), the two sublattices shift along the antiparallel directions relative to the midplane and exhibit a reversible spontaneous polarization Ps ≈ 3 μC·cm^{-2} with polar axis perpendicular to the layer plane [127]. Belianinov et al. [128] experimentally revealed ferroelectricity in CIPS flakes down to 50 nm at room temperature as evidenced by PFM studies.

Piezo-response force microscopy (PFM) is a widely used tool for nanoscale ferroelectric characterization [129]. The PFM amplitude reflects the absolute magnitude of the local piezoelectric response, while the phase indicates the polarization direction of each individual domain. With the assistance of this powerful tool, it is shown that switchable spontaneous polarization can exist in CIPS as thin as 4 nm [130]. As shown in Figure 15(c)–(e), distinct two-colour tones with a contrast of 180° are observed within the domain patterns, which evolve from fractal like structure in thinner flakes to dendrite-like in thicker flakes. Moreover, the well-defined butterfly loops of the PFM amplitude signals and the distinct 180° switching of the phase signals also prove the present of a robust ferroelectricity in CIPS ultrathin flakes (Figure 15(f)). A ferroelectric diode is fabricated in the form of Si/CIPS (30 nm)/Au (Figure 15(g)). A clear large hysteresis and resistive switching is observed, indicating that CIPS is a promising candidate for

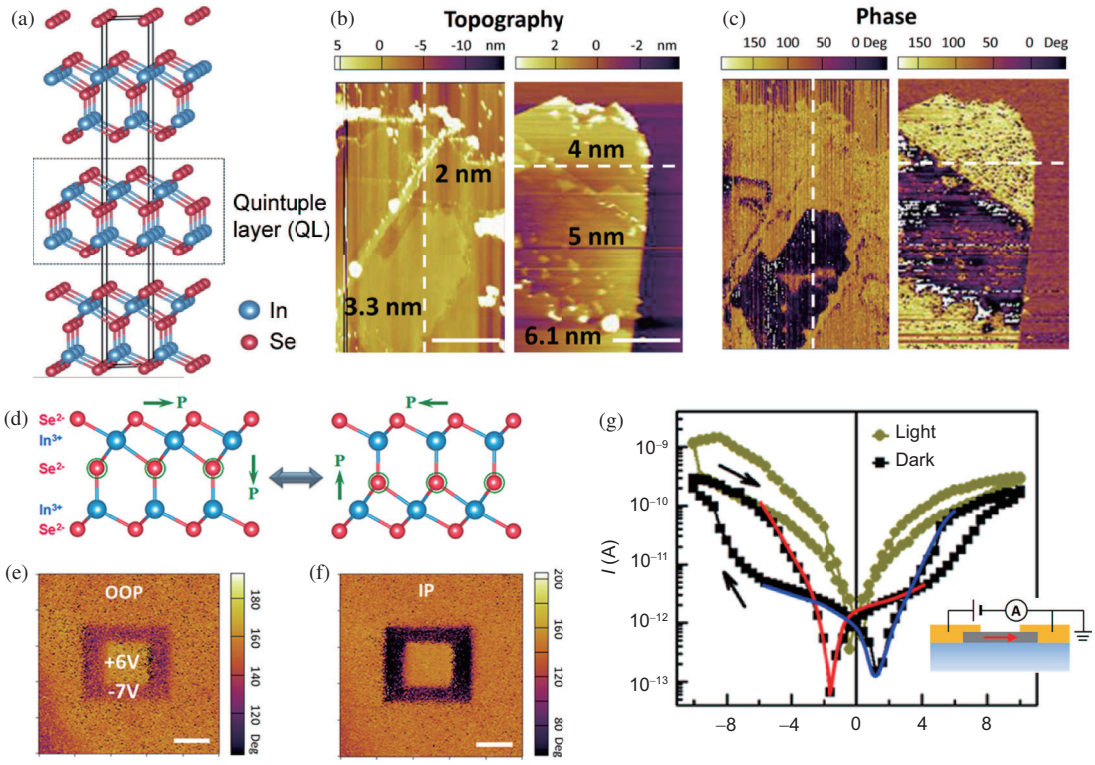

Figure 16 (Color online) Crystal structure and the ferroelectric characters of α-In_2Se_3 flakes. (a) Schematic model of IP and OOP switching coupling. (b) and (c) AFM and the corresponding IP PFM images of In_2Se_3 thin flakes. (d) Schematic model of intercorrelated OOP and IP switching. (e) OOP phase image and (f) the corresponding IP phase image of a 6 nm thick In_2Se_3 flake acquired immediately after writing two square patterns with a size of 2 and 1 mm by applying −7 and +6 V voltages consecutively. The scale bar is 1 mm. (g) *I*-*V* curves and schematic structure of the planar In_2Se_3 device. The red and blue solid lines are used to guide the eyes. Reproduced from [135] @Copyright 2017 Springer Nature.

the future of non-volatile electronics and offers an opportunity to be integrated with the well-established Si-based platforms.

Si et al. [131] fabricated ferroelectric field-effect transistors (Fe-FETs) with dual-gate structure based on CIPS and MoS_2 vdW heterostructure. Here, a 0.4 μm CIPS is used as the ferroelectric gate insulator. By sweeping the voltage from −5 V to 5 V, clear hysteresis loops can be seen in the transfer characteristics, demonstrating the nonvolatile memory property of the device. Furthermore, the performance of the MoS_2/CIPS Fe-FET can be modulated by a back gate. By employing a more negative VBG, a larger hysteresis loop can be observed.

Recently, In_2Se_3 is found to be one of a novel ferroelectric material, because it possesses both semiconducting and ferroelectric properties, rendering a possibility for the integration of nonvolatile memories into semiconductor wafers. In_2Se_3 has shown a great potential in technological applications, such as phase-change memory, thermoelectric, and optoelectronics [132–134]. Moreover, Ding et al. [135] predicted that In_2Se_3 and other III2-VI3 vdW materials may be ferroelectric semiconductors with both intrinsic in-plane and out-of-plane electric polarization at room-temperature. The first-principle calculations suggest that the In_2Se_3 possesses the lowest energy with a variant symmetry breaking Zincblende/Wurtzite crystal structure (Figure 16(a)). The lateral movement of Se atoms in the middle layer leads to the switching of the OOP (out-of-plane) and IP (in-plane) polarizations simultaneously. In other words, both polarizations are intercorrelated (Figure 16(b)). This discovery has stimulated intense experimental studies to validate this prediction. However, challenges still remain to fully understand the ferroelectricity of InxSey, owing to its polymorphism and complex phase diagram [136].

The crystal structure and OOP ferroelectricity of α-In_2Se_3 are confirmed by STEM, second-harmonic generation, and PFM characterization [137]. In addition, Cui et al. [138] demonstrated the generation

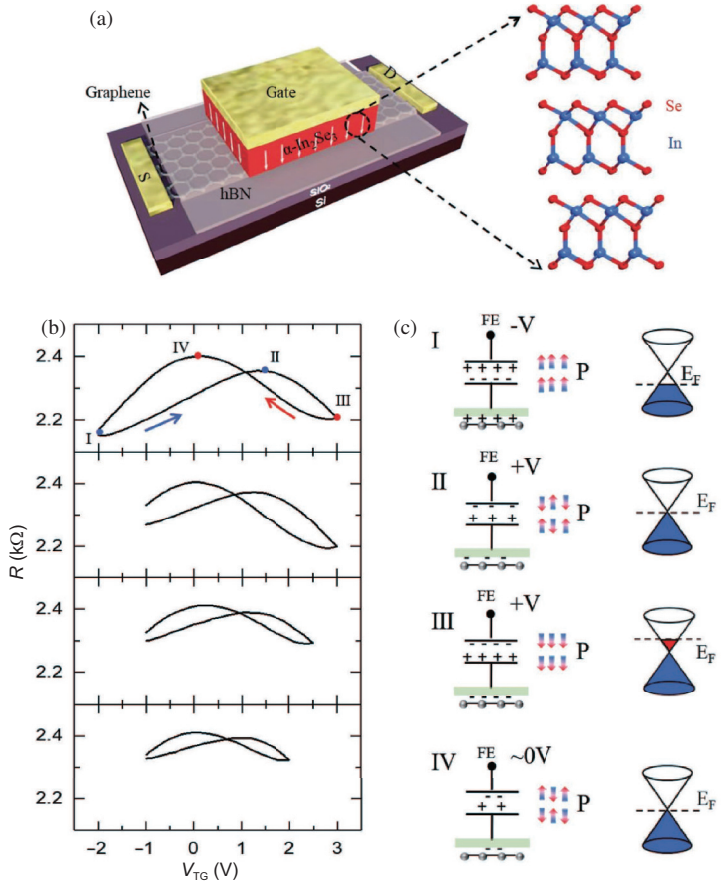

Figure 17 (Color online) Nonvolatile ferroelectric memory effect in 2D α-In_2Se_3. (a) 3D schematic model of the Fe-FET. The Fe-FET is fabricated by vertically stacking grapheme, h-BN, and In_2Se_3 thin layers in sequence. The white arrows indicate the direction of electric polarization. The zoomed area shows the crystal structure of ferroelectric In_2Se_3. (b) The hysteresis ferroelectric gating in 2D α-In_2Se_3 based Fe-FET device. The electrical hysteresis loop can be enlarged by the range of the applied top gate voltage. (c) Equivalent capacitor model of the 2D Fe-FET and the corresponding doping level in graphene. A capacitor is used to represent the top ferroelectric gate. The light green slab stands for the insulating h-BN layer. The small color arrows represent the electric dipoles in α-In_2Se_3. Reproduced from [140] @Copyright 2019 WILEY-VCH.

of a robust intercorrelated IP and OOP ferroelectricity in ultrathin CVD-grown α-In_2Se_3 with thickness down to 2 nm. As shown in Figure 16(b) and (c), clear ferroelectric domains are observed in ultrathin α-In_2Se_3 flakes with a thickness down to 2 nm. Interestingly, the IP phase changes simultaneously with the OOP phase, indicating that the IP polarization is intercorrelated with the OOP polarization (Figure 16(e) and (f)). According to the theoretical calculations [135], this unique IP and OOP intercorrelation could intrinsically originate from electric field-induced lateral movement of the central Se atomic layer (Figure 16(d)). Furthermore, the combination of the ferroelectric and semiconductive properties may expose a wealth of latent potential as demonstrated by a planar device (Figure 16(g)).

Almost simultaneously, Xiao et al. [139] verified this intercorrelated ferroelectricity through second harmonic generation spectroscopy (SHG) and PFM. Furthermore, as evidenced by the temperature-dependent SHG results, the ferroelectric phase of α-In_2Se_3 exhibits a high ferroelectric transition temperature of $\sim$700 K, which is partially owing to the large kinetic transition barrier involving both the IP and OOP reconfiguration.

Wan et al. [140] demonstrated the stable nonvolatile ferroelectric memory effect in a 2D Fe-FET with a α-In_2Se_3/h-BN/graphene structure, as shown in Figure 17(a). Benefit from the ferroelectric nature of α-In_2Se_3, as different electric dipoles would dope graphene with different types of carriers; the transfer curves are nonlinear and hysteretic (Figure 17(b) and (c)). The difference of the maximum resistance state

on the gate voltage is owing to the requirement of the coercive electric filed (Ec) for the reversal of the ferroelectric domains in α-In_2Se_3. Meanwhile, in order to quantitatively estimate the electric polarization of ultrathin α-In_2Se_3, they carry out dual-gating electrical measurements. With an equivalent capacitor divider model, the maximum induced electric polarization in α-In_2Se_3 is estimated to be 0.92 $\mu C{\cdot}cm^{-2}$.

Owing to a significant screening effect, ferroelectricity is exceedingly unusual to be found in metals [141, 142]. Besides, the screening effect also excludes external fields, ruling out the possibility of ferroelectric switching. However, Fei et al. [143] found that although the monolayer 1T'-WTe_2 is centrosymmetric and thus non-polarized, its stacked bulk structure is polarized. Moreover, switchable spontaneous OOP polarization could exist in metallic bilayer or trilayer 1T'-WTe_2 which is thin enough to allow electric field to penetrate through [143]. They fabricated devices made of thin WTe_2 flakes sandwiched between two h-BN with top and bottom gate. When sweeping the electrical field upwards and downwards, the conductance of the trilayer and bilayer devices shows bistability which is a characteristic of ferroelectric switching. However, as for devices based on monolayer WTe_2, no bistability is oberved, which is consistent with its centro-symmetric structure. To further confirm such bistability is related to the electric polarization, devices with top gate electrodes replaced by monolayer graphene are fabricated and measured. As the conductance of monolayer graphene is sensitive to the precise electric fields in the upper h-BN, it reflects the influence of the bottom gate on WTe_2. The dependence between the conductance of the monolayer graphene and the bottom electric field is very weak, which implies the conducting nature of WTe_2. Moreover, two stable terraces are observed, indicating the existence of two different vertical charge distributions in WTe_2, which further prove the OOP electric polar in WTe_2.

As the sister compound of WTe_2, recently, $MoTe_2$ has attracted a lot of attention owing to its rich physics and potential applications. Similarly to In_2Se_3, $MoTe_2$ exists in many crystal structures with very different electronic properties [144, 145]. 2H-$MoTe_2$ is semiconducting while 1T'-$MoTe_2$ (monoclinic (P21/m) structure) and T_d-$MoTe_2$ (orthorhombic ($Pmn2_1$)) are metallic and semi-metallic, respectively. Interestingly, Yuan et al. [146] found that 2H-$MoTe_2$ turns into distorted 1T (d1T) $MoTe_2$ which exhibits room-temperature OOP ferroelectricity down to one single layer upon laser irradiation. PFM studies are used to confirm the ferroelectricity in d1T-$MoTe_2$. As shown in Figure 18(a), clear phase and amplitude PFM hysteretic loops are observed, indicating a ferroelectric nature. Furthermore, a distinct phase contrast in the phase image can be observed, which is another proof of the existence of ferroelectricity in d1T-$MoTe_2$ (Figure 18(b)). Theoretical calculations, cross-sectional aberration-corrected scanning transmission electron microscopy (AC-STEM) as well as the second harmonic generation studies are further performed to investigate the origin of the OOP ferroelectricity in d1T-$MoTe_2$ (Figure 18(c)–(e)). The results reveal that the structure of d1T-$MoTe_2$ is distorted and a few Te atoms move towards the Mo plane along the OOP direction. Such non-centrosymmetric structure with vertical atomic displacement of Te leads to the spontaneous polarization.

Up to now, diverse 2D vdW materials have been predicted to be ferroelectric, such as the monolayer of 1-T MoS_2 [147], the monolayer group-IV monochalcogenides [148–150], the group III-V binary monolayers [151, 152], and bismuth oxychalcogenide [153]. Interestingly, most of these ferroelectrics are semiconductors with moderate bandgaps and high mobility [154–156]. These 2D ferroelectric materials thus hold great promise in potential applications.

Bulk MX (M = Ge, Sn; X = S, Se) possess a layered orthorhombic structure (space group Pnma) at room temperature, which can be derived from a 3D distortion of the NaCl structure [157]. Fei et al. [148] carried out first-principles calculations to investigate the ferroelectricity in monolayer group-IV monochalcogenides. For monolayer MXs, as shown in Figure 19(a), two stable structures labeled by B and B$'$ are noncentrosymmetric. Free-energy contour shown in Figure 19(b) confirms that these two structures (B and B$'$) are connected through a saddle point (A), such anharmonic double-well potential strongly indicates the existence of ferroelectricity.

Meanwhile, DFT calculations suggest that these two structures have significant spontaneous in-plane polarization with opposite polarizing directions. However, for the MXs with an even-number-of-layers MXs, the polarization is always zero. This is attributed to the restored inversion symmetry. In addition, the authors emploied Monte Carlo (MC) simulations to investigate the phase transition in these materials.

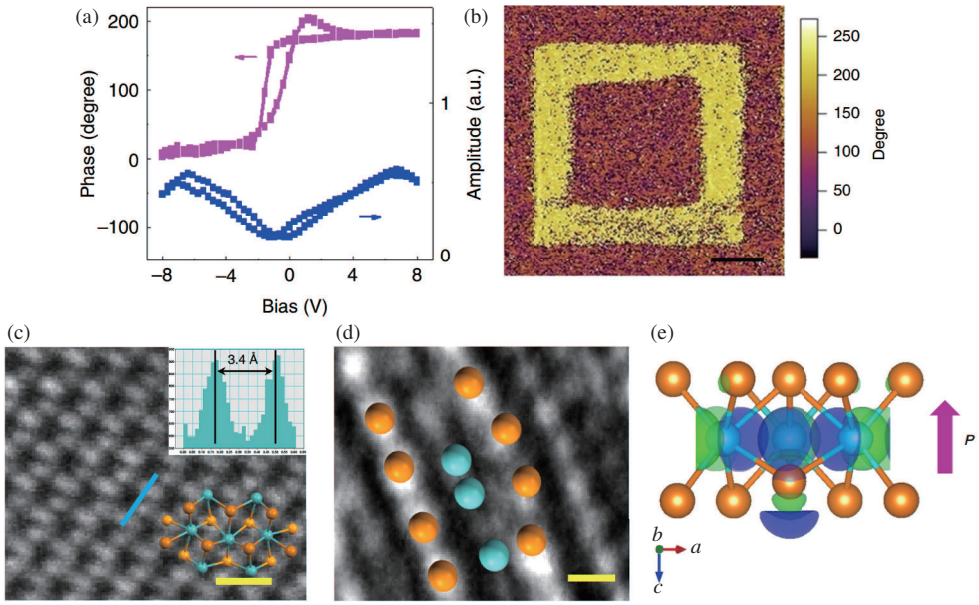

Figure 18 (Color online) Out-of-plane ferroelectricity in d1T-$MoTe_2$. (a) PFM phase hysteretic and butterfly loops of monolayer d1T-$MoTe_2$. (b) PFM phase image of monolayer d1T-$MoTe_2$. (c) Top-view HRTEM image and intensity profile with the atomic structure of d1T-$MoTe_2$ placed on top, scale bar, 0.5 nm. (d) Atomic structure image of monolayer d1T-$MoTe_2$ and the inset shows atomic structure model (cyan and orange colors represent Mo and Te atoms, respectively), scale-bar, 2 Å. (e) Side-view of charge density difference between ferroelectric d1T and paraelectric 1T phases (green, purple, cyan, orange, and pink colors denote negative charge, positive charge, Mo atom, Te atom, and polarization, respectively). Reproduced from [146] @Copyright 2019 WILEY-VCH.

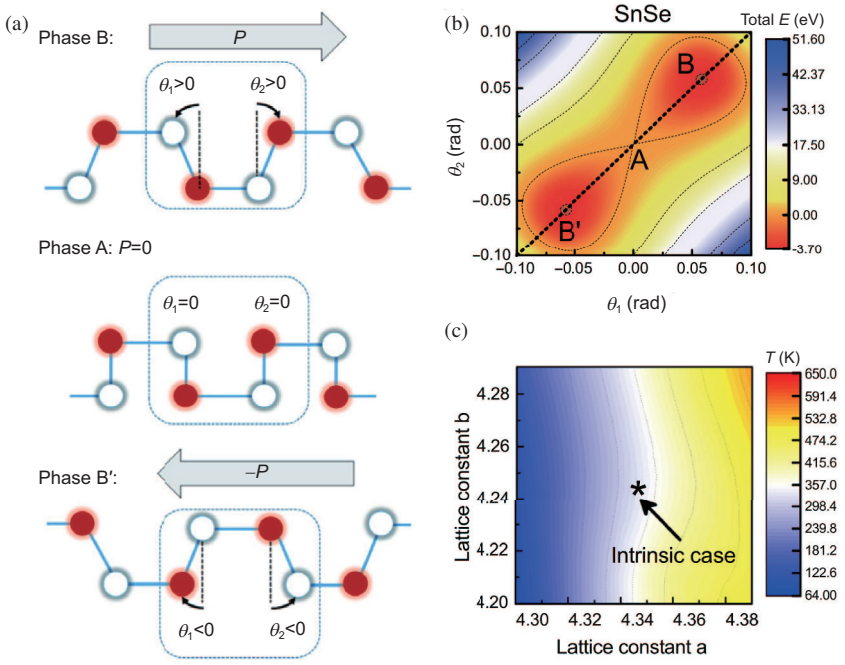

Figure 19 (Color online) Ferroelectricity in monolayer group-IV monochalcogenides. (a) The schematic side views of the two distorted degenerate polar structures (B and B′) and the high symmetry nonpolar phase (A). (b) The free-energy contour plot of monolayer SnSe according to the tilting angles (θ_1 and θ_2). The phases A, B, and B′ are marked. (c) Phase diagram of monolayer SnSe under strain. Reproduced from [148] @Copyright 2016 American Physical Society.

The calculated Curie Temperature (T_C) is above room temperature and could be tuned largely by a minor strain (Figure 19(c)). Much attention has been attracted in such systems, for the investigations of

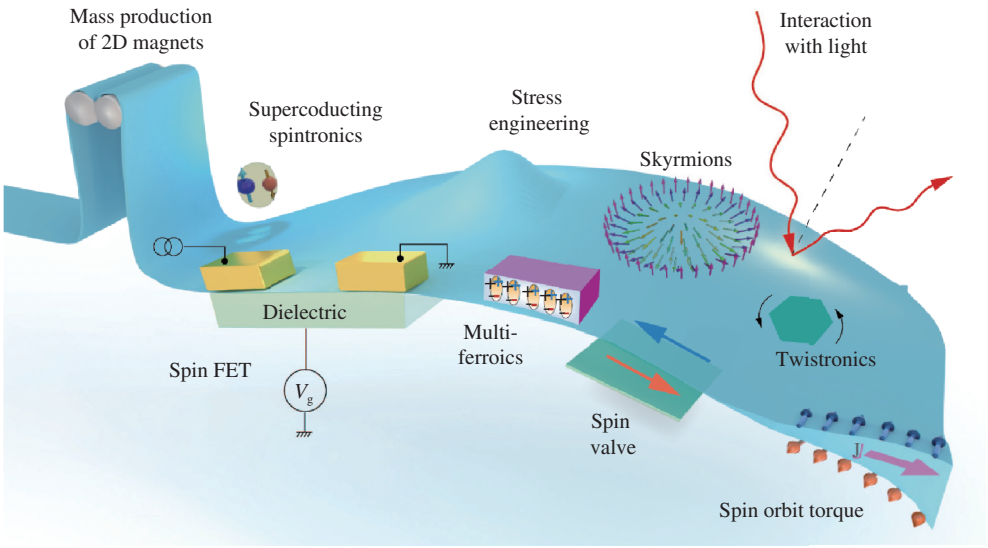

Figure 20 (Color online) Schematic vision of the future applications of two-dimensional materials with ferroic orderings.

interesting properties including domain wall motion, valley swapping [126].

4 Conclusion

As a summarization, two dimensional ferroic orderings have been a growingly new topic in solid state physics. A better understanding of the spin and/or dipole interactions in these new materials is one of the cutting-edge issues in condense matter physics. For example, fractal domain walls were observed in $Cr_2Ge_2Te_6$ and may trigger new discussions in the field [158]. Moreover recent studies, such as micro-scale investigations of the magnetic signals using single-spin microscopy, have revealed a magnetization of 16 $\mu B/nm^2$ in monolayer CrI_3 [159].

In general, with the dimension lowered from conventional 3D to 2D, spin interactions are confined within a flat atomic playground, giving rise to tremendous opportunities in nanotechnological applications as well as in the development of novel model devices in the fields of sensors and wearable electronics. For instant, in the atomically thin limit for semiconducting ferromagnetic or ferroelectric materials, new functions have been emerging, such as gate tunable, lattice twistable, flexible, mechanically stackable nature, potentially mass producible [160, 161]. As illustrated in Figure 20, it is foreseen that once the mass production of 2D magnets or ferroic films is realized, large sacle fabrication of sensor arrays of spin field effect transistors, spin valves, multi-ferroic devices can be acheived. Moreover, the handling of twistronics, as well as opto-electronics, can also be carried out in a macro-scale.

Most exciting nature about the 2D ferromagnetic and ferroelectric materials is that they can be assembled as desired: the number of stacking layers, the thickness of each layer, and the rotational angle between layers. It thus makes the 2D ferroic orderings an ideal platform for implementing 2D spin field effect transistors, 2D superconducting spintronics, 2D multi-ferroics, 2D spin valves, 2D magnetic/ferroelectric twistronics, and optoelectronics. As illustrated in Figure 20, 2D ferroic orderings are believed to open the door to new revolutionary technologies in the near future. Predictably, 2D multi-ferroic devices can be used for high-efficiency information reading, storage, and processing, which are of great significance for information industrial applications.

Acknowledgements This work was supported by National Key R&D Program of China (Grant No. 2017YFA0206302), and National Natural Science Foundation of China (Grant Nos. 11504385, 51627801, 61435010, 51702219, 61975134). Han ZHANG and Yupeng ZHANG acknowledge the support from Science and Technology Innovation Commission of Shenzhen (Grant Nos. JCYJ20170818093453105, JCYJ20180305125345378). Teng YANG acknowledges supports from Major Program of Aerospace Advanced Manufacturing Technology Research Foundation NSFC and CASC, China (Grant

No. U1537204). Zheng Vitto HAN acknowledges the support from Program of State Key Laboratory of Quantum Optics and Quantum Optics Devices (Grant No. KF201816).

References

1 Jiang X T, Liu S X, Liang W Y, et al. Broadband nonlinear photonics in few-layer MXene $Ti_3C_2T_x$ (T = F, O, or OH). Laser Photonics Rev, 2018, 12: 1700229
2 Lu L, Liang Z M, Wu L M, et al. Few-layer bismuthene: sonochemical exfoliation, nonlinear optics and applications for ultrafast photonics with enhanced stability. Laser Photonics Rev, 2018, 12: 1700221
3 Mu H R, Wang Z T, Yuan J, et al. Graphene-Bi_2Te_3 heterostructure as saturable absorber for short pulse generation. ACS Photonics, 2015, 2: 832–841
4 Lu L, Tang X, Cao R, et al. Broadband nonlinear optical response in few-layer antimonene and antimonene quantum dots: a promising optical kerr media with enhanced stability. Adv Opt Mater, 2017, 5: 1700301
5 Jiang Y Q, Miao L L, Jiang G B, et al. Broadband and enhanced nonlinear optical response of MoS_2/graphene nanocomposites for ultrafast photonics applications. Sci Rep, 2015, 5: 16372
6 Xing C Y, Jing G H, Liang X, et al. Graphene oxide/black phosphorus nanoflake aerogels with robust thermo-stability and significantly enhanced photothermal properties in air. Nanoscale, 2017, 9: 8096–8101
7 Zibouche N, Philipsen P, Kuc A, et al. Transition-metal dichalcogenide bilayers: Switching materials for spintronic and valleytronic applications. Phys Rev B, 2014, 90: 125440
8 Xiao D, Liu G B, Feng W, et al. Coupled spin and valley physics in monolayers of MoS_2 and other group-VI dichalcogenides. Phys Rev Lett, 2012, 108: 196802
9 Schaibley J R, Yu H, Clark G, et al. Valleytronics in 2D materials. Nat Rev Mater, 2016, 1: 16055
10 Sun Z B, Zhao Y T, Li Z B, et al. TiL_4-coordinated black phosphorus quantum dots as an efficient contrast agent for in vivo photoacoustic imaging of cancer. Small, 2017, 13: 1602896
11 Xie H H, Li Z B, Sun Z B, et al. Metabolizable ultrathin Bi_2Se_3 nanosheets in imaging-guided photothermal therapy. Small, 2016, 12: 4136–4145
12 Qi J, Lan Y W, Stieg A Z, et al. Piezoelectric effect in chemical vapour deposition-grown atomic-monolayer triangular molybdenum disulfide piezotronics. Nat Commun, 2015, 6: 7430
13 Li F, Qi J J, Xu M X, et al. Layer dependence and light tuning surface potential of 2D MoS_2 on various substrates. Small, 2017, 13: 1603103
14 Ren X H, Zhou J, Qi X, et al. Few-layer black phosphorus nanosheets as electrocatalysts for highly efficient oxygen evolution reaction. Adv Energy Mater, 2017, 7: 1700396
15 Wang T, Guo Y L, Wan P B, et al. Flexible transparent electronic gas sensors. Small, 2016, 12: 3748–3756
16 Xu C, Wang L B, Liu Z B, et al. Large-area high-quality 2D ultrathin Mo_2C superconducting crystals. Nat Mater, 2015, 14: 1135–1141
17 Liu Y, Weiss N O, Duan X D, et al. Van der Waals heterostructures and devices. Nat Rev Mater, 2016, 1: 16042
18 Novoselov K S, Mishchenko A, Carvalho A, et al. 2D materials and van der Waals heterostructures. Science, 2016, 353: aac9439
19 Manzeli S, Ovchinnikov D, Pasquier D, et al. 2D transition metal dichalcogenides. Nat Rev Mater, 2017, 2: 17033
20 Hu J M, Chen L Q, Nan C W. Multiferroic heterostructures integrating ferroelectric and magnetic materials. Adv Mater, 2016, 28: 15–39
21 Gong C, Zhang X. Two-dimensional magnetic crystals and emergent heterostructure devices. Science, 2019, 363: eaav4450
22 Gibertini M, Koperski M, Morpurgo A F, et al. Magnetic 2D materials and heterostructures. Nat Nanotechnol, 2019, 14: 408–419
23 Mermin N D, Wagner H. Absence of ferromagnetism or antiferromagnetism in one- or two-dimensional isotropic heisenberg models. Phys Rev Lett, 1966, 17: 1133–1136
24 Stanley H E, Kaplan T A. Possibility of a phase transition for the two-dimensional heisenberg model. Phys Rev Lett, 1966, 17: 913–915
25 Kosterlitz J M, Thouless D J. Ordering, metastability and phase transitions in two-dimensional systems. J Phys C-Solid State Phys, 1973, 6: 1181–1203
26 Berezinskii V L. Destruction of long-range order in one-dimensional and two-dimensional systems having a continuous symmetry group I. classical systems. J Exp Theor Phys, 1971, 32: 493
27 Fröhlich J, Lieb E H. Existence of phase transitions for anisotropic heisenberg models. Phys Rev Lett, 1977, 38: 440–442
28 Mohn P. Magnetism in the Solid State: An Introduction. Berlin: Springer, 2005
29 Blundell S. Magnetism in Condensed Matter. Oxford: Oxford University Press, 2001
30 Huang B, Clark G, Navarro-Moratalla E, et al. Layer-dependent ferromagnetism in a van der Waals crystal down to the monolayer limit. Nature, 2017, 546: 270–273
31 Gong C, Li L, Li Z L, et al. Discovery of intrinsic ferromagnetism in two-dimensional van der Waals crystals. Nature, 2017, 546: 265–269
32 Wang Z, Zhang T Y, Ding M, et al. Electric-field control of magnetism in a few-layered van der Waals ferromagnetic semiconductor. Nat Nanotech, 2018, 13: 554–559
33 Cao Y, Fatemi V, Demir A, et al. Correlated insulator behaviour at half-filling in magic-angle graphene superlattices.

Nature, 2018, 556: 80–84
34 Fei Z, Huang B, Malinowski P, et al. Two-dimensional itinerant ferromagnetism in atomically thin Fe_3GeTe_2. Nat Mater, 2018, 17: 778–782
35 Samarth N. Condensed-matter physics: magnetism in flatland. Nature, 2017, 546: 216–218
36 Tsubokawa I. On the magnetic properties of a $CrBr_3$ single crystal. J Phys Soc Jpn, 1960, 15: 1664–1668
37 Hansen W N. Some magnetic properties of the chromium (III) halides at 42 K. J Appl Phys, 1959, 30: S304
38 Starr C, Bitter F, Kaufmann A R. The magnetic properties of the iron group anhydrous chlorides at low temperatures. I. experimental. Phys Rev, 1940, 58: 977–983
39 Hansen W N, Griffel M. Heat capacities of CrF_3 and $CrCl_3$ from 15 to 300°K. J Chem Phys, 1958, 28: 902–907
40 Cable J W, Wilkinson M K, Wollan E O. Neutron diffraction investigation of antiferromagnetism in $CrCl_3$. J Phys Chem Solids, 1961, 19: 29–34
41 McGuire M A. Crystal and magnetic structures in layered, transition metal dihalides and trihalides. Crystals, 2017, 7: 121
42 Carteaux V, Moussa F, Spiesser M. 2D ising-like ferromagnetic behaviour for the lamellar $Cr_2Si_2Te_6$ compound: a neutron scattering investigation. Europhys Lett, 1995, 29: 251–256
43 Ouvrard G, Brec R, Rouxel J. Structural determination of some MPS_3 layered phases (M = Mn, Fe, Co, Ni and Cd). Mater Res Bull, 1985, 20: 1181–1189
44 Taylor B, Steger J, Wold A, et al. Preparation and properties of iron phosphorus triselenide, $FePSe_3$. Inorg Chem, 1974, 13: 2719–2721
45 Lado J L, Fernández-Rossier J. On the origin of magnetic anisotropy in two dimensional CrI_3. 2D Mater, 2017, 4: 035002
46 Ji H, Stokes R A, Alegria L D, et al. A ferromagnetic insulating substrate for the epitaxial growth of topological insulators. J Appl Phys, 2013, 114: 114907
47 Brec R. Review on structural and chemical properties of transition metal phosphorus trisulfides MPS_3. In: Intercalation in Layered Materials. Boston: Springer, 1986. 148: 93–124
48 Wildes A R, Simonet V, Ressouche E, et al. The magnetic properties and structure of the quasi-two-dimensional antiferromagnet $CoPS_3$. J Phys-Condens Matter, 2017, 29: 455801
49 Joy P A, Vasudevan S. Magnetism in the layered transition-metal thiophosphates MPS_3 (M=Mn, Fe, and Ni). Phys Rev B, 1992, 46: 5425–5433
50 Kurosawa K, Saito S, Yamaguchi Y. Neutron diffraction study on $MnPS_3$ and $FePS_3$. J Phys Soc Jpn, 1983, 52: 3919–3926
51 Deng Y J, Yu Y J, Song Y C, et al. Gate-tunable room-temperature ferromagnetism in two-dimensional Fe_3GeTe_2. Nature, 2018, 563: 94–99
52 Nozaki H, Umehara M, Ishizawa Y, et al. Magnetic properties of V_5S_8 single crystals. J Phys Chem Solids, 1978, 39: 851–858
53 Niu J J, Yan B M, Ji Q Q, et al. Anomalous Hall effect and magnetic orderings in nanothick V_5S_8. Phys Rev B, 2017, 96: 075402
54 Bonilla M, Kolekar S, Ma Y, et al. Strong room-temperature ferromagnetism in VSe_2 monolayers on van der Waals substrates. Nat Nanotech, 2018, 13: 289–293
55 Gong S J, Gong C, Sun Y Y, et al. Electrically induced 2D half-metallic antiferromagnets and spin field effect transistors. Proc Natl Acad Sci USA, 2018, 115: 8511–8516
56 Arai M, Moriya R, Yabuki N, et al. Construction of van der Waals magnetic tunnel junction using ferromagnetic layered dichalcogenide. Appl Phys Lett, 2015, 107: 103107
57 Wang X, Tang J, Xia X, et al. Current driven magnetization switching in a van der Waals ferromagnet Fe_3GeTe_2. 2019. ArXiv: 190205794v1
58 Wang Z, Sapkota D, Taniguchi T, et al. Tunneling spin valves based on Fe_3GeTe_2/hBN/Fe_3GeTe_2 van der Waals heterostructures. Nano Lett, 2018, 18: 4303–4308
59 Handy L L, Gregory N W. Structural properties of chromium (III) iodide and some chromium (III) mixed halides. J Am Chem Soc, 1952, 74: 891–893
60 Morosin B, Narath A. X-ray diffraction and nuclear quadrupole resonance studies of chromium trichloride. J Chem Phys, 1964, 40: 1958–1967
61 Huang B, Clark G, Klein D R, et al. Electrical control of 2D magnetism in bilayer CrI_3. Nat Nanotech, 2018, 13: 544–548
62 Ghazaryan D, Greenaway M T, Wang Z, et al. Magnon-assisted tunnelling in van der Waals heterostructures based on CrBr3. Nat Electron, 2018, 1: 344–349
63 Zhang W B, Qu Q, Zhu P, et al. Robust intrinsic ferromagnetism and half semiconductivity in stable two-dimensional single-layer chromium trihalides. J Mater Chem C, 2015, 3: 12457–12468
64 Dillon Jr J F, Kamimura H, Remeika J P. Magneto-optical properties of ferromagnetic chromium trihalides. J Phys Chem Solids, 1966, 27: 1531–1549
65 Wang H, Eyert V, Schwingenschlögl U. Electronic structure and magnetic ordering of the semiconducting chromium trihalides $CrCl_3$, $CrBr_3$, and CrI_3. J Phys-Condens Matter, 2011, 23: 116003
66 Wang H B, Fan F R, Zhu S S, et al. Doping enhanced ferromagnetism and induced half-metallicity in CrI_3 monolayer. EPL, 2016, 114: 47001
67 Sivadas N, Okamoto S, Xu X, et al. Stacking-dependent magnetism in bilayer CrI3. Nano Lett, 2018, 18: 7658–7664

68 Webster L, Yan J A. Strain-tunable magnetic anisotropy in monolayer $CrCl_3$, $CrBr_3$, and CrI_3. Phys Rev B, 2018, 98: 144411

69 Zheng F W, Zhao J Z, Liu Z, et al. Tunable spin states in the two-dimensional magnet CrI_3. Nanoscale, 2018, 10: 14298–14303

70 McGuire M A, Dixit H, Cooper V R, et al. Coupling of crystal structure and magnetism in the layered, ferromagnetic insulator CrI_3. Chem Mater, 2015, 27: 612–620

71 Song T, Cai X, Tu M W Y, et al. Giant tunneling magnetoresistance in spin-filter van der Waals heterostructures. Science, 2018, 360: 1214–1218

72 Wang Z, Gutiérrez-Lezama I, Ubrig N, et al. Very large tunneling magnetoresistance in layered magnetic semiconductor CrI_3. Nat Commun, 2018, 9: 2516

73 Klein D R, MacNeill D, Lado J L, et al. Probing magnetism in 2D van der Waals crystalline insulators via electron tunneling. Science, 2018, 360: 1218–1222

74 Jiang S W, Li L Z, Wang Z F, et al. Controlling magnetism in 2D CrI_3 by electrostatic doping. Nat Nanotech, 2018, 13: 549–553

75 Jiang S W, Shan J, Mak K F. Electric-field switching of two-dimensional van der Waals magnets. Nat Mater, 2018, 17: 406–410

76 Valenzuela S O, Roche S. A barrier to spin filters. Nat Electron, 2018, 1: 328–329

77 Richter N, Weber D, Martin F, et al. Temperature-dependent magnetic anisotropy in the layered magnetic semiconductors CrI_3 and $CrBr_3$. Phys Rev Mater, 2018, 2: 024004

78 Yu X Y, Zhang X, Shi Q, et al. Large magnetocaloric effect in van der Waals crystal $CrBr_3$. Front Phys, 2019, 14: 43501

79 Thompson S E, Parthasarathy S. Moore's law: the future of Si microelectronics. Mater Today, 2006, 9: 20–25

80 Story T, Gałązka R R, Frankel R B, et al. Carrier-concentration-induced ferromagnetism in PbSnMnTe. Phys Rev Lett, 1986, 56: 777–779

81 Ohno H, Chiba D, Matsukura F, et al. Electric-field control of ferromagnetism. Nature, 2000, 408: 944–946

82 Sivadas N, Daniels M W, Swendsen R H, et al. Magnetic ground state of semiconducting transition-metal trichalcogenide monolayers. Phys Rev B, 2015, 91: 235425

83 Xing W Y, Chen Y Y, Odenthal P M, et al. Electric field effect in multilayer $Cr_2Ge_2Te_6$: a ferromagnetic 2D material. 2D Mater, 2017, 4: 024009

84 Carteaux V, Brunet D, Ouvrard G, et al. Crystallographic, magnetic and electronic structures of a new layered ferromagnetic compound $Cr_2Ge_2Te_6$. J Phys-Condens Matter, 1995, 7: 69–87

85 Zhang X, Zhao Y L, Song Q, et al. Magnetic anisotropy of the single-crystalline ferromagnetic insulator $Cr_2Ge_2Te_6$. Jpn J Appl Phys, 2016, 55: 033001

86 Tian Y, Gray M J, Ji H W, et al. Magneto-elastic coupling in a potential ferromagnetic 2D atomic crystal. 2D Mater, 2016, 3: 025035

87 Dong X J, You J Y, Gu B, et al. Strain-induced room-temperature ferromagnetic semiconductors with giant anomalous Hall effect in two-dimensional $Cr_2Ge_2Te_6$. 2019. ArXiv: 190109306

88 Wang K Y, Hu T, Jia F H, et al. Magnetic and electronic properties of $Cr_2Ge_2Te_6$ monolayer by strain and electric-field engineering. Appl Phys Lett, 2019, 114: 092405

89 Xie L, Guo L, Yu W Z, et al. Ultrasensitive negative photoresponse in 2D $Cr_2Ge_2Te_6$ photodetector with light-induced carrier trapping. Nanotechnology, 2018, 29: 464002

90 He J J, Ding G Q, Zhong C Y, et al. Remarkably enhanced ferromagnetism in a super-exchange governed $Cr_2Ge_2Te_6$ monolayer via molecular adsorption. J Mater Chem C, 2019, 7: 5084–5093

91 Lohmann M, Su T, Niu B, et al. Probing magnetism in insulating $Cr_2Ge_2Te_6$ by induced anomalous Hall effect in Pt. Nano Lett, 2019, 19: 2397–2403

92 Miao N H, Xu B, Zhu L G, et al. 2D intrinsic ferromagnets from van der Waals antiferromagnets. J Am Chem Soc, 2018, 140: 2417–2420

93 Lançon D, Ewings R A, Guidi T, et al. Magnetic exchange parameters and anisotropy of the quasi-two-dimensional antiferromagnet $NiPS_3$. Phys Rev B, 2018, 98: 134414

94 ur Rehman Z, Muhammad Z, Adetunji Moses O, et al. Magnetic isotropy/anisotropy in layered metal phosphorous trichalcogenide MPS_3 (M = Mn, Fe) single crystals. Micromachines, 2018, 9: 292

95 Haines C R S, Coak M J, Wildes A R, et al. Pressure-induced electronic and structural phase evolution in the van der Waals compound $FePS_3$. Phys Rev Lett, 2018, 121: 266801

96 Kim K, Lim S Y, Lee J U, et al. Suppression of magnetic ordering in XXZ-type antiferromagnetic monolayer $NiPS_3$. Nat Commun, 2019, 10: 345

97 Qi J S, Wang H, Chen X F, et al. Two-dimensional multiferroic semiconductors with coexisting ferroelectricity and ferromagnetism. Appl Phys Lett, 2018, 113: 043102

98 Cai L, He J F, Liu Q H, et al. Vacancy-induced ferromagnetism of MoS_2 nanosheets. J Am Chem Soc, 2015, 137: 2622–2627

99 Feng S M, Lin Z, Gan X, et al. Doping two-dimensional materials: ultra-sensitive sensors, band gap tuning and ferromagnetic monolayers. Nanoscale Horiz, 2017, 2: 72–80

100 Cheng Y C, Zhu Z Y, Mi W B, et al. Prediction of two-dimensional diluted magnetic semiconductors: doped monolayer MoS_2 systems. Phys Rev B, 2013, 87: 100401

101 Ramasubramaniam A, Naveh D. Mn-doped monolayer MoS_2: an atomically thin dilute magnetic semiconductor.

Phys Rev B, 2013, 87: 195201
102 Fan X L, An Y R, Guo W J. Ferromagnetism in transitional metal-doped MoS_2 monolayer. Nanoscale Res Lett, 2016, 11: 154
103 Xia B R, Guo Q, Gao D Q, et al. High temperature ferromagnetism in Cu-doped MoS_2 nanosheets. J Phys D-Appl Phys, 2016, 49: 165003
104 Wang Y, Tseng L T, Murmu P P, et al. Defects engineering induced room temperature ferromagnetism in transition metal doped MoS_2. Mater Des, 2017, 121: 77–84
105 Li B, Xing T, Zhong M Z, et al. A two-dimensional Fe-doped SnS_2 magnetic semiconductor. Nat Commun, 2017, 8: 1958
106 Radhakrishnan S, Das D, Samanta A, et al. Fluorinated h-BN as a magnetic semiconductor. Sci Adv, 2017, 3: e1700842
107 Jiang P H, Li L, Liao Z L, et al. Spin direction-controlled electronic band structure in two-dimensional ferromagnetic CrI_3. Nano Lett, 2018, 18: 3844–3849
108 O'Hara D J, Zhu T, Trout A H, et al. Room temperature intrinsic ferromagnetism in epitaxial manganese selenide films in the monolayer limit. Nano Lett, 2018, 18: 3125–3131
109 Mounet N, Gibertini M, Schwaller P, et al. Two-dimensional materials from high-throughput computational exfoliation of experimentally known compounds. Nat Nanotech, 2018, 13: 246–252
110 Freitas D C, Weht R, Sulpice A, et al. Ferromagnetism in layered metastable 1T-$CrTe_2$. J Phys-Condens Matter, 2015, 27: 176002
111 Lin M W, Zhuang H L, Yan J, et al. Ultrathin nanosheets of $CrSiTe_3$: a semiconducting two-dimensional ferromagnetic material. J Mater Chem C, 2016, 4: 315–322
112 Kong T, Stolze K, Timmons E I, et al. VI3-a New layered ferromagnetic semiconductor. Adv Mater, 2019, 31: 1808074
113 Tong Q J, Liu F, Xiao J, et al. Skyrmions in the Moiré of van der Waals 2D magnets. Nano Lett, 2018, 18: 7194–7199
114 Asadi K, de Leeuw D M, de Boer B, et al. Organic non-volatile memories from ferroelectric phase-separated blends. Nat Mater, 2008, 7: 547–550
115 Cross L E. Ferroelectric materials for electromechanical transducer applications. Mater Chem Phys, 1996, 43: 108–115
116 Muralt P. Ferroelectric thin films for micro-sensors and actuators: a review. J Micromech Microeng, 2000, 10: 136–146
117 Wang Y, Niranjan M K, Janicka K, et al. Ferroelectric dead layer driven by a polar interface. Phys Rev B, 2010, 82: 094114
118 Duan C G, Sabirianov R F, Mei W N, et al. Interface effect on ferroelectricity at the nanoscale. Nano Lett, 2006, 6: 483–487
119 Jia C L, Nagarajan V, He J Q, et al. Unit-cell scale mapping of ferroelectricity and tetragonality in epitaxial ultrathin ferroelectric films. Nat Mater, 2007, 6: 64–69
120 Junquera J, Ghosez P. Critical thickness for ferroelectricity in perovskite ultrathin films. Nature, 2003, 422: 506–509
121 Zhang Y, Li G P, Shimada T, et al. Disappearance of ferroelectric critical thickness in epitaxial ultrathin $BaZrO_3$ films. Phys Rev B, 2014, 90: 184107
122 Kooi B J, Noheda B. Ferroelectric chalcogenides–materials at the edge. Science, 2016, 353: 221–222
123 Chang K, Liu J, Lin H, et al. Discovery of robust in-plane ferroelectricity in atomic-thick SnTe. Science, 2016, 353: 274–278
124 Liu K, Lu J, Picozzi S, et al. Intrinsic origin of enhancement of ferroelectricity in SnTe ultrathin films. Phys Rev Lett, 2018, 121: 027601
125 Yang C, Liu Y Y, Tang G, et al. Non-monotonic thickness dependence of Curie temperature and ferroelectricity in two-dimensional SnTe film. Appl Phys Lett, 2018, 113: 082905
126 Maisonneuve V, Cajipe V B, Simon A, et al. Ferrielectric ordering in lamellar $CuInP_2S_6$. Phys Rev B, 1997, 56: 10860–10868
127 Vysochanskii Y M, Stephanovich V A, Molnar A A, et al. Raman spectroscopy study of the ferrielectric-paraelectric transition in layered $CuInP_2S_6$. Phys Rev B, 1998, 58: 9119–9124
128 Belianinov A, He Q, Dziaugys A, et al. $CuInP_2S_6$Room temperature layered ferroelectric. Nano Lett, 2015, 15: 3808–3814
129 Vasudevan R K, Balke N, Maksymovych P, et al. Ferroelectric or non-ferroelectric: why so many materials exhibit "ferroelectricity" on the nanoscale. Appl Phys Rev, 2017, 4: 021302
130 Liu F, You L, Seyler K L, et al. Room-temperature ferroelectricity in $CuInP_2S_6$ ultrathin flakes. Nat Commun, 2016, 7: 12357
131 Si M, Liao P Y, Qiu G, et al. Ferroelectric field-effect transistors based on MoS_2 and $CuInP_2S_6$ two-dimensional van der Waals heterostructure. ACS Nano, 2018, 12: 6700–6705
132 Lee H, Kang D H, Tran L. Indium selenide (In_2Se_3) thin film for phase-change memory. Mater Sci Eng-B, 2005, 119: 196–201
133 Han G, Chen Z G, Drennan J, et al. Indium selenides: structural characteristics, synthesis and their thermoelectric performances. Small, 2014, 10: 2747–2765
134 Island J O, Blanter S I, Buscema M, et al. Gate controlled photocurrent generation mechanisms in high-gain In_2Se_3Phototransistors. Nano Lett, 2015, 15: 7853–7858
135 Ding W J, Zhu J B, Wang Z, et al. Prediction of intrinsic two-dimensional ferroelectrics in In_2Se_3 and other III_2-VI_3 van der Waals materials. Nat Commun, 2017, 8: 14956

136 Ye J, Soeda S, Nakamura Y, et al. Crystal structures and phase transformation in In_2Se_3 compound semiconductor. Jpn J Appl Phys, 1998, 37: 4264–4271

137 Zhou Y, Wu D, Zhu Y H, et al. Out-of-plane piezoelectricity and ferroelectricity in layered α-In_2Se_3 nanoflakes. Nano Lett, 2017, 17: 5508–5513

138 Cui C, Hu W J, Yan X, et al. Intercorrelated in-plane and out-of-plane ferroelectricity in ultrathin two-dimensional layered semiconductor In_2Se_3. Nano Lett, 2018, 18: 1253–1258

139 Xiao J, Zhu H Y, Wang Y, et al. Intrinsic two-dimensional ferroelectricity with dipole locking. Phys Rev Lett, 2018, 120: 227601

140 Wan S, Li Y, Li W, et al. Nonvolatile ferroelectric memory effect in ultrathin α-In_2Se_3. Adv Funct Mater, 2019, 29: 1808606

141 Shi Y G, Guo Y F, Wang X, et al. A ferroelectric-like structural transition in a metal. Nat Mater, 2013, 12: 1024–1027

142 Kim T H, Puggioni D, Yuan Y, et al. Polar metals by geometric design. Nature, 2016, 533: 68–72

143 Fei Z, Zhao W, Palomaki T A, et al. Ferroelectric switching of a two-dimensional metal. Nature, 2018, 560: 336–339

144 Keum D H, Cho S, Kim J H, et al. Bandgap opening in few-layered monoclinic $MoTe_2$. Nat Phys, 2015, 11: 482–486

145 Qi Y, Naumov P G, Ali M N, et al. Superconductivity in Weyl semimetal candidate $MoTe_2$. Nat Commun, 2016, 7: 11038

146 Yuan S, Luo X, Chan H L, et al. Room-temperature ferroelectricity in $MoTe_2$ down to the atomic monolayer limit. Nat Commun, 2019, 10: 1775

147 Shirodkar S N, Waghmare U V. Emergence of ferroelectricity at a metal-semiconductor transition in a 1T monolayer of MoS_2. Phys Rev Lett, 2014, 112: 157601

148 Fei R X, Kang W, Yang L. Ferroelectricity and phase transitions in monolayer group-IV monochalcogenides. Phys Rev Lett, 2016, 117: 097601

149 Wang H, Qian X F. Two-dimensional multiferroics in monolayer group IV monochalcogenides. 2D Mater, 2017, 4: 015042

150 Hanakata P Z, Carvalho A, Campbell D K, et al. Polarization and valley switching in monolayer group-IV monochalcogenides. Phys Rev B, 2016, 94: 035304

151 Şahin H, Cahangirov S, Topsakal M, et al. Monolayer honeycomb structures of group-IV elements and III-V binary compounds: First-principles calculations. Phys Rev B, 2009, 80: 155453

152 Blonsky M N, Zhuang H L, Singh A K, et al. Ab initio prediction of piezoelectricity in two-dimensional materials. ACS Nano, 2015, 9: 9885–9891

153 Wu M, Zeng X C. Bismuth oxychalcogenides: a new class of ferroelectric/ferroelastic materials with ultra high mobility. Nano Lett, 2017, 17: 6309–6314

154 Wu J X, Yuan H T, Meng M M, et al. High electron mobility and quantum oscillations in non-encapsulated ultrathin semiconducting Bi_2O_2Se. Nat Nanotech, 2017, 12: 530–534

155 Yoon S M, Song H J, Choi H C. p-type semiconducting GeSe combs by a vaporization-condensation-recrystallization (VCR) process. Adv Mater, 2010, 22: 2164–2167

156 Mukherjee B, Cai Y, Tan H R, et al. NIR Schottky photodetectors based on individual single-crystalline GeSe nanosheet. ACS Appl Mater Interfaces, 2013, 5: 9594–9604

157 Zhao L D, Lo S H, Zhang Y, et al. Ultralow thermal conductivity and high thermoelectric figure of merit in SnSe crystals. Nature, 2014, 508: 373–377

158 Guo T F, Ma Z W, Lin G T, et al. Multiple structure and symmetry types in narrow temperature and magnetic field ranges in two-dimensional $Cr_2Ge_2Te_6$ crystal. 2018. ArXiv: 180306113

159 Thiel L, Wang Z, Tschudin M A, et al. Probing magnetism in 2D materials at the nanoscale with single-spin microscopy. Science, 2019, 364: 973–976

160 Cheng R Q, Wang F, Yin L, et al. High-performance, multifunctional devices based on asymmetric van der Waals heterostructures. Nat Electron, 2018, 1: 356–361

161 Wang F, Wang Z X, Yin L, et al. 2D library beyond graphene and transition metal dichalcogenides: a focus on photodetection. Chem Soc Rev, 2018, 47: 6296–6341